MAKING THE DARK MATTER CONNECTION BETWEEN PARTICLE PHYSICS AND COSMOLOGY

A Dissertation

by

ABRAM MICHAEL KRISLOCK

Submitted to the Office of Graduate Studies of
Texas A&M University
in partial fulfillment of the requirements for the degree of

DOCTOR OF PHILOSOPHY

August 2011

Major Subject: Physics

MAKING THE DARK MATTER CONNECTION BETWEEN PARTICLE PHYSICS AND COSMOLOGY

A Dissertation

by

ABRAM MICHAEL KRISLOCK

Submitted to the Office of Graduate Studies of
Texas A&M University
in partial fulfillment of the requirements for the degree of

DOCTOR OF PHILOSOPHY

Approved by:

Chair of Committee,	Bhaskar Dutta
Committee Members,	Teruki Kamon
	Dimitri Nanopoulos
	Stephen Fulling
Head of Department,	Ed Fry

August 2011

Major Subject: Physics

ABSTRACT

Making the Dark Matter Connection Between Particle Physics and Cosmology.
(August 2011)

Abram Michael Krislock, B.S., University of Regina
Chair of Advisory Committee: Dr. Bhaskar Dutta

Dark matter has been shown to be extremely abundant in our universe. It comprises about 23% of the energy density of the entire universe, which is more than five times greater than the regular matter we already know about. Dark matter cannot be explained within the Standard Model of particle physics. However, models which extend the Standard Model, such as supersymmetry, can explain dark matter. This dissertation investigates the signals of some supersymmetry models in the context of collider physics. If dark matter particles or other supersymmetry particles are produced at some collider experiment, such as the Large Hadron Collider, it is important to know how we can find and measure the signatures and properties of these particles. This dissertation provides some measurement techniques for that exact purpose. These measurement techniques are also very general, making them useful for examining other models of particle physics as well. Lastly, if the supersymmetry model can be understood well enough from collider data, the connection back to cosmology can be made. Namely, it is possible to determine (from LHC data and using a standard cosmological calcuation) the abundance of dark matter in the universe. Comparing this collider value with the value already measured will be a crucial step in understanding dark matter. This dissertation provides simulated results of this dark matter abundance calculation for a number of supersymmetry model points.

TABLE OF CONTENTS

LIST OF FIGURES

LIST OF TABLES

1 INTRODUCTION

The Standard Model (SM) of particle physics describes our world remarkably well. All of the matter we see and interact with in this world can be described by it. However, we have seen that there exists other matter in our universe as well. The energy density of the universe has recently been determined very accurately by the Wilkinson Microwave Anisotropy Probe (WMAP) [1] to be 23% dark matter and 73% Dark Energy. This leaves only 4% of the content of the energy density of the universe which can be explained by the SM of particle physics.

This SM describes that 4% of our universe remarkably well. The particles of the SM consist of *fermions* which are the building blocks of all the matter we have seen. These fermions consist of *quarks* and *leptons*. The most famous quarks are those that form the basic structures of all our atoms. These quarks are the *up* and *down* quarks, u and d, which combine to form the protons and neutrons of all the atoms in the universe. Additionally, two other generations of quarks have been discovered. These are the second generation *charm* and *strange* quarks, c and s, as well as the third generation *top* and *bottom* quarks, t and b. The leptons of the SM also show up in pairs and in three generations like the quarks. The first generation includes the well known *electron* and its corresponding *electron neutrino*, e and ν_e. The second and third generation of leptons are the *muon* and *muon neutrino*, μ and ν_μ, and the *tauon* and *tauon neutrino*, τ and ν_τ. All of these SM fermions have been summarized in Table 1.

This dissertation follows the style of Physics Review D.

Table 1: SM Particles. The fermions of the SM as well as the SM gauge and Higgs bosons. The SM fermions appear as denoted in the text. The right-handed helicity state of the neutrino, ν_R, does not appear here since it is neutral under all SM gauge forces and, thus, does not interact in the SM at all.

$\begin{pmatrix} u \\ d \end{pmatrix}_L$	u_R d_R	$\begin{pmatrix} e \\ \nu_e \end{pmatrix}_L$	e_R	$[g]_8$	W_1 W_2 W_3	B	H^0
$\begin{pmatrix} c \\ s \end{pmatrix}_L$	c_R s_R	$\begin{pmatrix} \mu \\ \nu_\mu \end{pmatrix}_L$	μ_R				
$\begin{pmatrix} t \\ b \end{pmatrix}_L$	t_R b_R	$\begin{pmatrix} \tau \\ \nu_\tau \end{pmatrix}_L$	τ_R				

The SM also contains *gauge bosons* which mediate the forces that the fermions feel. These forces are called *gauge forces* and are governed by *gauge groups.* The gauge groups of the SM are $\mathrm{SU(3)_C}$, $\mathrm{SU(2)_L}$, and $\mathrm{U(1)_Y}$. The gauge group $\mathrm{SU(3)_C}$ governs the *strong force* which is felt by particles with *color charge*, such as the quarks. This strong force is responsible for the binding of quarks together to form the nuclei of atoms. The gauge boson for this group is the *gluon*, g, which is the particle which mediates the strong force between the quarks. There are eight gluons to mediate the forces of different colored particles. The gauge groups $\mathrm{SU(2)_L}$ and $\mathrm{U(1)_Y}$ jointly govern the *electroweak* force. The gauge group $\mathrm{SU(2)_L}$ governs the force felt by *left-handed helicity states* of the fermions which form pairs of particles such as (u_L, d_L), or $(e_L, \nu_{e,L})$. It has three W gauge bosons to mediate these forces. The last gauge group $\mathrm{U(1)_Y}$ governs the force which is felt by any particle with *hypercharge*, and has one B gauge boson to mediate this force. These gauge bosons have also been summarized in Table 1.

Lastly, the SM also predicts a Higgs boson, yet to be discovered, which is responsible for the electroweak breaking mechanism. This mechanism breaks the electroweak force down into the *electromagnetic* and *weak* forces. The gauge groups break as $\mathrm{SU(2)_L} \times \mathrm{U(1)_Y} \rightarrow \mathrm{U(1)_{EM}}$, and their gauge bosons undergo a transformation. The gauge boson for the surviving gauge group $\mathrm{U(1)_{EM}}$ is the *photon*, γ, which remains massless. The photon now mediates the *electromagnetic* force felt by electrically charged particles. The other gauge bosons of the broken group recombine to form the massive gauge bosons, W^+, W^-, and Z^0, which govern the weak force. These bosons have gained their mass due to the breaking of their symmetry group. In this process, the Higgs boson also gives mass to all the SM fermions. The Higgs boson is also listed with the other SM particles in Table 1.

Regardless of how wonderful a description of these particles the SM provides, dark matter cannot be explained by the SM. From WMAP as well as other observations, we know some properties about the dark matter particle. Since we have never yet detected it directly on Earth, we know it does not feel the strong force, or else it would have interacted with the protons and neutrons of our world. Thus it must be color neutral. We cannot see it, so it must not interact with light (photons). Thus, it must be electrically neutral as well. Since it is still a large part of our universe today it must be stable. Lastly, it must also be massive to get the current dark matter content of the universe correct. These properties are all supported by the recent observation of the bullet cluster [2]. In that famous picture, we can see a clear separation of luminous matter from dark matter as the two galaxies collide. The luminous matter has slowed down due to strong and electomagnetic forces after the collision of the galaxies, and it remains near the center of the galactic collision. The dark matter, which can be detected only by gravitational lensing effects, does not slow down much at all. The dark matter seen in the picture has moved significantly further away from the collision point than the luminous matter. This observation reaffirms the properties which dark matter must have: Neutrality, stability, only weak interaction, and massiveness. There are no such particles available in the SM which have these four properties.

However, dark matter can be explained by a variety of models which extend the SM. Supersymmetry (SUSY) [3] is one such model which provides a natural dark matter candidate particle. SUSY also provides crucial fixes to some of the problems inherent in the SM. The basic version of the SUSY model introduces a SUSY transformation which transforms fermions to bosons and bosons to fermions in the Lagrangian. To make this transformation a *symmetry* of the model, there is an additional SUSY fermion for each SM boson, as well as an additional SUSY boson for each SM fermion introduced to the model. The spin-1/2 fermions of the SM,

Table 2: SM and SUSY Particles. The particles of the SM as well as their corresponding SUSY superpartners. The SUSY sfermions appear just as the SM fermions, but are denoted with a tilde overtop. The charginos and neutralinos, which are superpartners of the gauge and Higgs bosons, are denoted with a $\widetilde{\chi}$. All particles shown are the mass eigenstates. The L and R subscripts of the sfermions do not denote helicity. Rather, these subscripts denote which SM helicity particle is the superpartner of the sfermion. Numbered subscripts denote mass eigenstates of the SUSY particles. The smaller numbered SUSY particles are less massive than the larger numbered SUSY particles of the same type.

$\begin{pmatrix}u\\d\end{pmatrix}_L$	u_R d_R	$\begin{pmatrix}e\\\nu_e\end{pmatrix}_L$	e_R	$\widetilde{u}_L$ $\widetilde{d}_L$	$\widetilde{u}_R$ $\widetilde{d}_R$	$\widetilde{e}_L$ $\widetilde{\nu}_{eL}$	$\widetilde{e}_R$
$\begin{pmatrix}c\\s\end{pmatrix}_L$	c_R s_R	$\begin{pmatrix}\mu\\\nu_\mu\end{pmatrix}_L$	μ_R	$\widetilde{c}_L$ $\widetilde{s}_L$	$\widetilde{c}_R$ $\widetilde{s}_R$	$\widetilde{\mu}_L$ $\widetilde{\nu}_{\mu L}$	$\widetilde{\mu}_R$
$\begin{pmatrix}t\\b\end{pmatrix}_L$	t_R b_R	$\begin{pmatrix}\tau\\\nu_\tau\end{pmatrix}_L$	τ_R	$\widetilde{t}_2$ $\widetilde{b}_2$	$\widetilde{t}_1$ $\widetilde{b}_1$	$\widetilde{\tau}_2$ $\widetilde{\nu}_{\tau L}$	$\widetilde{\tau}_1$
$[g]_8$	$W^\pm$ $H^\pm$	γ Z^0	h^0 H^0	$[\widetilde{g}]_8$	$\widetilde{\chi}_2^\pm$ $\widetilde{\chi}_1^\pm$	$\widetilde{\chi}_4^0$ $\widetilde{\chi}_3^0$	$\widetilde{\chi}_2^0$ $\widetilde{\chi}_1^0$

the quarks and leptons, each have a SUSY spin-0 boson *superpartner*. These superpartners of the fermions are called *sfermions*, or scalar fermions. Similarily, we refer to the scalar quarks and leptons as *squarks* and *sleptons*. SUSY also contains two Higgs boson doublets, compared to the SM which has only one. These SM gauge and Higgs bosons also have superpartners in the SUSY transformation called *gauginos* and *Higgsinos*. Although the gauge bosons have spin-1 and the Higgs bosons have spin-0, the gauginos and Higgsinos both have spin-1/2. Since they both have the same spin, the gauginos and Higgsinos in the model may mix together to form mass eigenstates. The electrically charged eigenstates are called *charginos*, while the electrically neutral eigenstates are called *neutralinos*. All of these SUSY particles are shown corresponding to their SM superpartners in Table 2

In SUSY models with R-parity conservation, interactions may only involve even numbers of SUSY partners of SM particles. Thus, any SUSY particle must decay into other SUSY particles, forcing the lightest one to be stable. In most SUSY models, the lightest, stable particle is the neutralino which is also neutral and only interacts via the weak force. This makes the neutralino an excellent dark matter candidate [4]. SUSY models based upon Supergravity Grand Unification [5] also solve many of the problems inherent in the SM.

These SUSY models predict a slew of new fundamental particles. In order to test these models, these particles must be discovered and have their masses measured. These mass measurements can be used in *bottom-up* studies [6] which distinguish between models and determine the model parameters. These bottom-up studies can be model-dependent or model-independent with pros and cons for each method. The model-independent studies are very general and can detect any SUSY model. However, very few things about the details of the model can be learned. On the other hand, the model-dependent studies require very specific signals to solve the model. However, these studies can uncover very general measurement techniques, while at the same time completely reconstruct certain models of SUSY.

This study is a bottom-up model-dependent examination of the effects of SUSY dark matter models at the Large Hadron Collider (LHC). The LHC is a proton-proton collider, which is currently running at a center of mass collision energy of 7 TeV. There are two major experiments running at the LHC which will search for the Higgs boson as well as physics beyond the SM. These are the ATLAS [7] and CMS [8] experiments. Both of these experiments can detect leptons (e, μ), photons (γ), certain τ leptons, *missing transverse energy*, $\not{E}_{\rm T}$, (coming from particles which do not interact within the detector, and transverse to the incoming beam direction), and *jets*. Jets are created whenever a SM quark (other than the top quark, t) is produced in a decay. Since the strong force is so strong at the energy scales such as at the LHC, quarks can never be free. Thus, a quark which is a decay product immediately interacts and radiates gluons. These gluons then convert into particles of stable quark combinations called *hadrons*. The quark basically sprays a bunch of hadrons within the detector. Taking all of these hadrons together can basically reconstruct the original quark. The grouping of the hadrons from one quark is what is referred to as a jet.

These leptons, photons, τ's, $\not{E}_{\rm T}$, and jets are all the information which experiments at the LHC can give us in order to understand which particles were produced during the proton-proton collision. Thus, in order to find and measure the SUSY superpartners of SM particles, we must use this information to *reconstruct* the collision event to see what happened. In order to know how to do that, we must plan *physical observables* and *measurement techniques* to do just that. This study shows some options for such plans by performing Monte Carlo simulations of the experiments which will take place at the LHC to produce and discover these new particles. Although this study is model-dependent, these analysis techniques are general enough to apply to other models with similar signatures. This study also presents the method of using the mass measurements to determine the model parameters.

For this model-dependent study, once the model parameters have been determined by the measurements made at the LHC, we can infer the remaining SUSY particle masses. Having the full SUSY mass spectrum allows us to determine the current dark matter abundance in the universe, also known as the dark matter relic density. This provides a measure of the dark matter content of the universe which is from the LHC, and thus, independent of WMAP. This is how the connection between particle physics and cosmology is made, and is the main goal of this study.

The dark matter content of the universe can be calculated via use of the Boltzmann equation [9]:

$$\frac{\mathrm{d}n}{\mathrm{d}t} = -3Hn - \langle \sigma v \rangle \left(n^2 - n_{eq}^2 \right) . \tag{1.1}$$

This equation can be understood very easily. The number density of some species of particles in the universe is given by n. Its rate of change with time depends on the expansion rate of the universe, which is given by the Hubble parameter, $H = \dot{a}/a$, where a is the scale of the universe. As the universe expands, the volume of the universe increases, naturally decreasing the number density. This is shown as the first term on the right hand side of Equation (1.1). The number density rate of change also depends on the average annihilation cross-section times speed, $\langle \sigma v \rangle$, of the particle species.

According to the standard cosmology, in the early universe, just moments after the

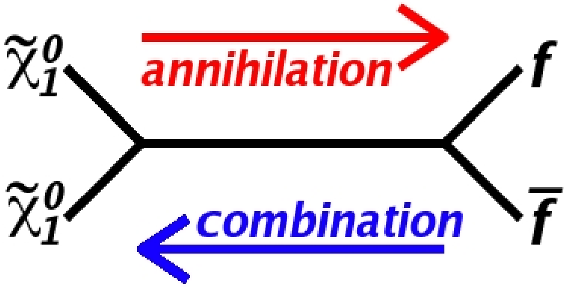

Figure 1: Dark Matter Annihilation. Annihilation of two dark matter particles into a fermion, anti-fermion pair. In the early universe, when all particles were still in thermal equilibrium, the reverse combination process was also occurring just as abundantly as the annihilation process.

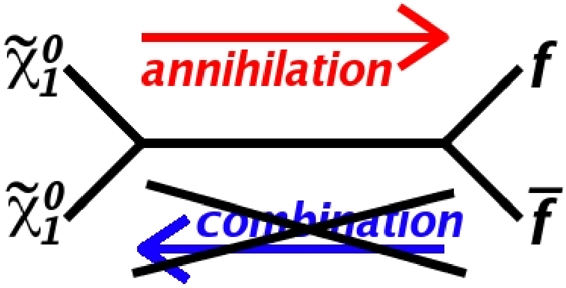

Figure 2: Dark Matter Freeze Out. Annihilation of two dark matter particles into a fermion, anti-fermion pair. After the freeze out of the massive dark matter particles, the reverse combination is no longer kinematically possible.

Big Bang, all the particles of the universe were in thermal equilibrium. Thus, if some particle species, $\tilde{\chi}_1^0$, annihilated into some other particles, f, then the reverse interaction also happened. Even if the f particles are much lighter than the $\tilde{\chi}_1^0$ particles, the f's have enough energy in the thermal equilibrium to recombine into the $\tilde{\chi}_1^0$ particles. This is depicted graphically in Figure 1. This situation can be understood in Equation (1.1) by taking $n_{eq} \simeq n$. In this case, the annihilation cross-section does not affect the number density of the $\tilde{\chi}_1^0$ particles.

Once the universe expanded and cooled off, the f particles no longer had enough energy to recombine into the $\tilde{\chi}_1^0$ particles. We think of this as the $\tilde{\chi}_1^0$ particles falling out of thermal equilibrium with the other particles. This situation is called

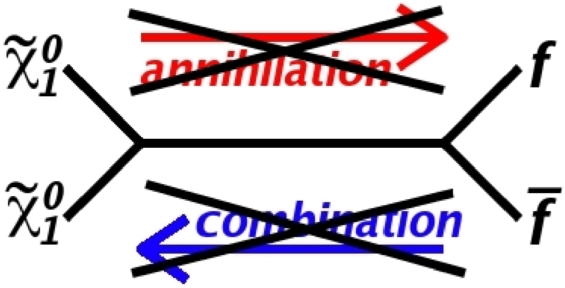

Figure 3: Dark Matter Relic. Annihilation of two dark matter particles into a fermion, anti-fermion pair. When the expansion rate of the universe becomes large enough, the dark matter particles can no longer annihilate, forming the dark matter relic content of the universe.

freeze out depicted graphically in Figure 2. Understanding the situation when the $\tilde{\chi}_1^0$ particles freeze out is possible by setting $n_{eq} \simeq 0$ in Equation (1.1). During the freeze out, the $\tilde{\chi}_1^0$ particles annihilate abundantly, decreasing their number density greatly.

Finally, there becomes a point in time where the Hubble expansion of the universe becomes much greater than the annihilation effect. In a sense, the universe expands so quickly, that the $\tilde{\chi}_1^0$ particles can no longer find each other in order to annihilate. Since the $\tilde{\chi}_1^0$ particles are no longer annihilating, if they are stable, they become a *relic*. For dark matter $\tilde{\chi}_1^0$ particles, we refer to the abundance of dark matter left in the universe today as dark matter *relic density*. This situation is depicted in Figure 3. In Equation (1.1), we can understand this by neglecting the entire $\langle\sigma v\rangle$ term.

Thus, the Boltzmann Equation (1.1) describes very well the behavior of the number density of dark matter in the universe, under a thermal equilibrium scenario. Given a model, we can use this equation to predict the dark matter content of the universe. As mentioned above, using a model reconstructed from measurements made at the LHC will give us an independent test of the WMAP result for the dark matter relic density of the universe.

Performing this study requires the use of multiple computing tools to set up the model and perform the LHC simulations. To generate the SUSY particle mass spectrum, a program called ISAJET [10] is used. Simulation of the production and subsequent decays of SUSY particles at the LHC is performed by a Monte Carlo program called PYTHIA [11]. The detector simulation is performed by another Monte Carlo program, PGS4 [12]. ROOT [13] is a framework of computing tools useful for the analysis of data. Lastly, to make the cosmological connection and determine the dark matter content of the universe, DARKSUSY [14] is used.

The starting point of these simulations is to choose a model for study. The very general Minimal Supersymmetric SM has just over one hundred model parameters which specify the mass spectrum. Thus, it would be impossible to determine this model entirely from measurements which can be made at the LHC. Instead, this study chooses a much simpler model to start with. The Minimal Supergravity (mSUGRA) [5] model is a well motivated SUSY extension of the SM. In mSUGRA, many of the SUSY particle masses unify at the Grand Unified (GUT) energy scale. At the GUT scale, the interaction strengths of the strong and electroweak forces unify. The mass unification at the GUT scale means that mSUGRA has only four parameters and a sign necessary to determine all the masses of the SUSY particles. These parameters are: (i) The unified mass of all scalar bosons at the GUT scale, m_0; (ii) the unified mass of gauginos at the GUT scale, $m_{1/2}$; (iii) the unified trilinear coupling between the Higgs and SUSY scalars at the GUT scale, A_0; (iv) the ratio of vacuum expectation values of the two Higgs bosons during the electroweak symmetry breaking, $\tan\beta$; (v) the sign of the bilinear Higgs coupling $\text{sign}(\mu)$.

These four parameters and a sign determine all of the masses of the SUSY superpartners of SM particles. The effect of the parameters on the different types of SUSY particles is very obvious, even at the low energy scale where the LHC experiment is performed. For instance, the first two generations of sleptons have masses which are determined mostly by m_0. The first two generations of squarks interact strongly, since they have color charge; they are also influenced by the gluino mass. Thus the squark masses are determined mostly by m_0 and $m_{1/2}$. The third generation squarks and sleptons interact much more strongly with the Higgs boson, as well as being involved in the trilinear coupling. Thus, the third generation squark and slepton masses are also determined by A_0 and $\tan\beta$. Lastly, the charginos and neutralinos are mixed eigenstates of the gauginos and neutralinos. Thus, their masses are determined by $m_{1/2}$, $\tan\beta$ and μ.

The possibilities of choices for these four parameters make up a parameter space. Within this parameter space, there are multiple regions which predict the correct amount of dark matter content of the universe. This study considers many of these regions in order to determine, for each region, the final state signals of particles at the LHC. These final state signals are then used to uniquely identify which region within the model is best verified by the signal as well as to determine the model parameters. Lastly, this study will take the results of the measured model parameters from the LHC simulations to determine how well the dark matter relic density of the universe can be determined at the LHC.

The remainder of this dissertation is organized as follows. In Section 2, the basic principles behind finding useful, measurable observables of SUSY particles at the LHC is discussed in detail. Some sample decay chains and their respective observables are investigated. In Section 3, powerful subtraction techniques which can help to remove large amounts of background from physical observables are described. In Section 4, these physical observables and subtraction techniques are employed in a sample of LHC simulations for different SUSY models based upon mSUGRA. Each signal is described, along with the observables and subtraction techniques used. The result for each model is shown, along with estimates of the resulting uncertainties in the model parameters and dark matter relic density. Finally, in Section 5, the major results are summarized. Also, outlooks on the future of these types of studies are discussed.

2 PHYSICAL OBSERVABLES

Our goal of understanding as much of any particle model as we can depends on our ability to make measurements from the collider. If SUSY exists, and SUSY particles are within reach at the LHC, then we will be able to find evidence of these particles within LHC collision events. SUSY particles which are produced from the collision will decay into SM particles and other SUSY particles. In SUSY models with R-parity, the SUSY particles continue to decay this way until one decay product is the lightest SUSY particle, which is stable. However, if this last SUSY particle is the dark matter candidate, it will be weakly interacting and escape detection at the LHC.

In order to make measurements of the SUSY particles, we must partially reconstruct such *decay chains*. In this way, we can measure the masses of the SUSY particles. With enough unique measurements, or physical observables, we can determine the masses of the major constituents of these decay chains. Alternatively, we can use the physical observables to measure the model parameters instead of the individual masses.

To construct useful physical observables, we examine the decay chains to look for signals where the SM decay products are detectable. Information about the SM particles, including their momenta and energies, is collected by the detector. This kinematical information can be combined in a way to provide information about the decays of the SUSY particles.

The most basic example of such a combination is to measure the mass of a particle which decays to two detectable particles. For now, consider the decay of the Z boson into an electron-positron pair. We can calculate the expected kinematics of this decay using special relativity. To do this, we simply conserve four-momentum in the rest frame of the Z boson.

$$(m_Z, 0, 0, 0) = (E_{e^+}, p_x, p_y, p_z) + (E_{e^-}, q_x, q_y, q_z)\,. \tag{2.1}$$

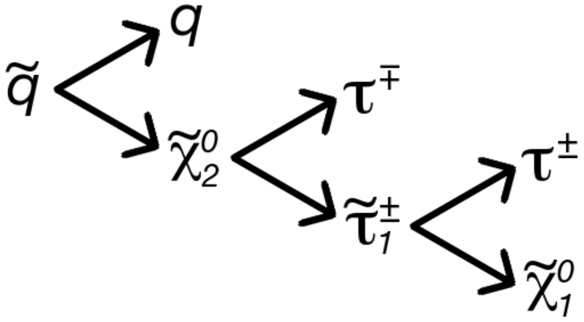

Figure 4: Jet-τ-τ Decay Chain. SUSY decay chain. A squark decays into a quark and the second lightest neutralino. This neutralino decays into a stau and a tau lepton. The stau then decays into another tau lepton and the lightest neutralino, which is stable. Conservation of charge requires that the two tau leptons have opposite charges.

In Equation (2.1), m_Z is the mass of the Z boson, and $\vec{p}$ ($\vec{q}$) and E_{e^+} (E_{e^-}) are the momentum and energy of the positron (electron). Natural units are taken with the speed of light, $c = 1$. In the rest frame of the Z boson, it has zero momentum, and its energy is simply its mass.

With this kinematic behavior in mind, we can calculate the *invariant mass* of the electron-positron pair, $m_{e^+e^-}$. This *invariant* mass is invariant under Lorentz transformations, so we can calculate it in any reference frame. In the rest frame of the Z boson, this invariant mass is trivial to calculate using the conservation of four-momentum (Eq. (2.1)):

$$m_{e^+e^-} = \sqrt{(E_{e^+} + E_{e^-})^2 - (\vec{p} + \vec{q})^2} = \sqrt{m_Z^2 + 0^2} = m_Z. \tag{2.2}$$

Thus, if we can identify the electron and positron coming from this Z boson, the Z boson can be fully reconstructed, which means its four-momentum is measured.

For a less trivial example, consider the SUSY decay chain shown in Fig. 4. Suppose we want to use the information from the two τ leptons in the figure to partially reconstruct the decay chain. Once again, we calculate the expected kinematics.

This time we start in the rest frame of the second lightest neutralino. To simplify the calculation we approximate the rest mass of the tau leptons to be zero. First we conserve four-momentum for the second lightest neutralino decay.

$$\left(m_{\tilde{\chi}_2^0}, 0, 0, 0\right) = \left(p_{\tau^\mp}, p_{\tau^\mp,x}, p_{\tau^\mp,y}, p_{\tau^\mp,z}\right) + \left(E_{\tilde{\tau}_1}, p_{\tilde{\tau}_{1,x}}, p_{\tilde{\tau}_{1,y}}, p_{\tilde{\tau}_{1,z}}\right). \tag{2.3}$$

We also conserve four-momentum for the decay of the stau.

$$\left(E_{\tilde{\tau}_1}, p_{\tilde{\tau}_{1,x}}, p_{\tilde{\tau}_{1,y}}, p_{\tilde{\tau}_{1,z}}\right) = \left(q_{\tau^\pm}, q_{\tau^\pm,x}, q_{\tau^\pm,y}, q_{\tau^\pm,z}\right) + \left(E_{\tilde{\chi}_1^0}, k_{\tilde{\chi}^0_{1,x}}, k_{\tilde{\chi}^0_{1,y}}, k_{\tilde{\chi}^0_{1,z}}\right). \tag{2.4}$$

From Equation (2.3), it is clear that the stau and tau decay products must be back to back. That is to say, $\vec{p}_{\tau^\mp} = -\vec{p}_{\tilde{\tau}_1^\pm} \equiv \vec{p}$. To clean up the notation, we drop the remaining particle subscripts and expand the energies in Equations (2.3) and (2.4):

$$\left(m_{\tilde{\chi}_2^0}, 0, 0, 0\right) = (p, p_x, p_y, p_z) + \left(\sqrt{m^2_{\tilde{\tau}_1} + p^2}, -p_x, -p_y, -p_z\right); \tag{2.5}$$

$$\left(\sqrt{m^2_{\tilde{\tau}_1} + p^2}, -p_x, -p_y, -p_z\right) = (q, q_x, q_y, q_z) + \left(\sqrt{m^2_{\tilde{\chi}_1^0} + k^2}, k_x, k_y, k_z\right). \tag{2.6}$$

Once again, our goal is to calculate the invariant mass, this time for the two tau leptons. The two tau invariant mass, $m_{\tau\tau}$, unfortunately cannot completely reconstruct the decay chain as was the case for the Z boson decay. We cannot fully reconstruct the decay chain because the lightest neutralino escapes detection. Instead, we consider what information can be gained under special circumstances of the decay chain. For instance, if we take θ as the angle between the momenta $\vec{p}$ and $\vec{q}$ of the two tau leptons, the invariant mass can be written as

$$\begin{aligned} m_{\tau\tau} &= \sqrt{(p+q)^2 - (\vec{p} + \vec{q})^2} && \text{(2.7a)} \\ &= \sqrt{p^2 + q^2 + 2pq - p^2 - q^2 - 2\vec{p} \cdot \vec{q}} && \text{(2.7b)} \\ &= \sqrt{2pq(1 - \cos\theta)}. && \text{(2.7c)} \end{aligned}$$

We can easily see from Equation (2.7c) that $m_{\tau\tau}$ has a natural maximum if $\theta = \pi$, that is, if the two tau leptons are back to back. With this assumption, all that is required to calculate the maximum two tau invariant mass, $m_{\tau\tau}^{\max}$, are the magnitudes of momenta p and q of the tau leptons.

The momentum p can be solved for rather easily from the energy component of Equation (2.5).

$$m_{\tilde{\chi}_2^0} = p + \sqrt{m_{\tilde{\tau}_1}^2 + p^2} \tag{2.8a}$$

$$\left(m_{\tilde{\chi}_2^0} - p\right)^2 = m_{\tilde{\tau}_1}^2 + p^2 \tag{2.8b}$$

$$m_{\tilde{\chi}_2^0}^2 + p^2 - 2m_{\tilde{\chi}_2^0} p = m_{\tilde{\tau}_1}^2 + p^2 \tag{2.8c}$$

$$p = \frac{m_{\tilde{\chi}_2^0}^2 - m_{\tilde{\tau}_1}^2}{2m_{\tilde{\chi}_2^0}}. \tag{2.8d}$$

Solving for the momentum q is more complicated, since we must eliminate the unmeasurable momentum of the lightest neutralino, $\vec{k}$. From Equation (2.6), we see that $\vec{k} = -\vec{p} - \vec{q}$. Using this, as well as Equation (2.8a), in the energy component of Equation (2.6) gives:

$$\sqrt{m_{\tilde{\tau}_1}^2 + p^2} = q + \sqrt{m_{\tilde{\chi}_1^0}^2 + k^2} \tag{2.9a}$$

$$m_{\tilde{\chi}_2^0} - p - q = \sqrt{m_{\tilde{\chi}_1^0}^2 + p^2 + q^2 + 2\vec{p}\cdot\vec{q}} \tag{2.9b}$$

$$\left(m_{\tilde{\chi}_2^0} - p - q\right)^2 = m_{\tilde{\chi}_1^0}^2 + p^2 + q^2 - 2pq \tag{2.9c}$$

$$m_{\tilde{\chi}_2^0}^2 - 2pm_{\tilde{\chi}_2^0}^2 - 2qm_{\tilde{\chi}_2^0}^2 + 2pq = m_{\tilde{\chi}_1^0}^2 - 2pq \tag{2.9d}$$

$$-2qm_{\tilde{\chi}_2^0}^2 + 4pqm_{\tilde{\chi}_2^0} = m_{\tilde{\chi}_2^0}(m_{\tilde{\chi}_1^0}^2 - m_{\tilde{\chi}_2^0}^2 + 2pm_{\tilde{\chi}_2^0}) \tag{2.9e}$$

$$-2qm_{\tilde{\tau}_1}^2 = m_{\tilde{\chi}_2^0}(m_{\tilde{\chi}_1^0}^2 - m_{\tilde{\tau}_1}^2) \tag{2.9f}$$

$$q = m_{\tilde{\chi}_2^0} \frac{m_{\tilde{\tau}_1}^2 - m_{\tilde{\chi}_1^0}^2}{2m_{\tilde{\tau}_1}^2} \tag{2.9g}$$

where we have once again used the fact that $\vec{p}$ and $\vec{q}$ are back to back. Thus,

$$m_{\tau\tau}^{\max} = \sqrt{4pq} = \sqrt{m_{\tilde{\chi}_2^0}^2 \left(1 - \frac{m_{\tilde{\tau}_1}^2}{m_{\tilde{\chi}_2^0}^2}\right)\left(1 - \frac{m_{\tilde{\chi}_1^0}^2}{m_{\tilde{\tau}_1}^2}\right)} \tag{2.10}$$

This maximum of the invariant mass of the two tau leptons from this decay chain is a very useful measurement. If we can somehow identify and collect the pairs of tau leptons from such decay chains for many events, we can make a histogram of $m_{\tau\tau}$. Such a histogram should show the maximum value, or *endpoint*, $m_{\tau\tau}^{\max}$. The measurement of this endpoint gives us information about the SUSY particle masses involved in the decay chain which produce the two tau leptons. According to Equation (2.10), we gain information about the masses of the lightest and second lightest neutralino, as well as the lighter stau.

We can construct many different physical observables using this *endpoint* measurement technique. For example, we can partially reconstruct the decay chain shown in Figure 4 with other invariant masses. In addition to $m_{\tau\tau}^{\max}$, there are two other endpoints which we can measure:

$$m_{J\tau}^{\max} = \sqrt{m_{\tilde{q}}^2 \left(1 - \frac{m_{\tilde{\chi}_2^0}^2}{m_{\tilde{q}}^2}\right)\left(1 - \frac{m_{\tilde{\tau}_1}^2}{m_{\tilde{\chi}_2^0}^2}\right)} \tag{2.11}$$

$$m_{J\tau\tau}^{\max} = \sqrt{m_{\tilde{q}}^2 \left(1 - \frac{m_{\tilde{\chi}_2^0}^2}{m_{\tilde{q}}^2}\right)\left(1 - \frac{m_{\tilde{\chi}_1^0}^2}{m_{\tilde{\chi}_2^0}^2}\right)} \tag{2.12}$$

These endpoints also give information about the masses of the SUSY particles involved in this decay chain. Here we note that Equation (2.12) is not as general as the others. When three particles are being reconstructed, there are different possibilities for the maximum configuration [15]. It is not as simple as saying that two particles must be back to back. However, as long as our study does not vary the masses too wildly, this Equation (2.12) remains valid within regions of parameter space which we are interested in.

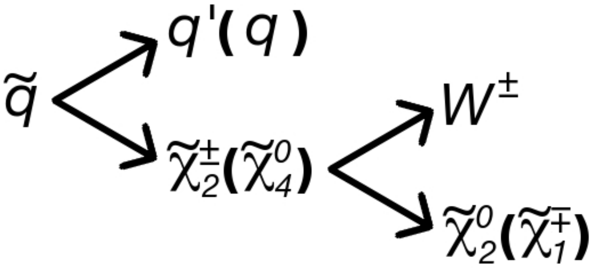

Figure 5: W-plus-Jet Decay Chain. SUSY decay chain. A squark decays into a quark and the heavier chargino (or the heaviest neutralino). This chargino (or neutralino) decays into the second lightest neutralino (or lighter chargino). Subsequently, the decay chain continues, but we need not consider it here.

There are other decay chains which may give rise to endpoint measurements such as these. Figure 5 shows another example of a SUSY decay chain which can be partially reconstructed. Again, we can use the information about the detectable particles to partially reconstruct the decay chain. The W boson decays to two quarks, yet can be reconstructed. Combining that W boson with the corresponding quark coming from the squark decay also results in an endpoint. The theoretical calculation of this endpoint is somewhat more involved than the previous endpoints due to the fact that the W boson has a non-negligible mass. The maximum endpoint for the decay chain shown in Figure 5 is shown in Equation (2.13):

$$m_{JW}^{\max} = m_{\tilde{\chi}_2^{\pm}} \sqrt{C + \frac{1}{2}\left(A-1\right)\left(1 + C - B + \sqrt{(1-C-B)^2 - 4BC}\right)}, \qquad (2.13)$$

where $A \equiv m_{\tilde{q}}^2/m_{\tilde{\chi}_2^{\pm}}^2$, $B \equiv m_{\tilde{\chi}_2^0}^2/m_{\tilde{\chi}_2^{\pm}}^2$, and $C \equiv m_W^2/m_{\tilde{\chi}_2^{\pm}}^2$. For the bracketed SUSY particles in the chain shown in Figure 5 the equation is the same with $m_{\tilde{\chi}_2^{\pm}} \to m_{\tilde{\chi}_4^0}$ and $m_{\tilde{\chi}_2^0} \to m_{\tilde{\chi}_1^{\mp}}$. There are very similar decay chains in some SUSY events involving Higgs boson or Z boson final states in place of the W boson. Those decays have the same endpoint as Equation (2.13) with different definitions for A, B, and C.

Lastly, there are kinematical observables we can construct other than invariant masses. We can get an idea for the energy of the overall SUSY scale simply by looking at events where the squarks decay immediately into the lightest neutralinos. Usually these events come from squark-gluino, gluino pair, or squark pair production. If we measure the energy of the quarks coming from the squark and gluino decays along with the missing energy from the neutralino escaping the detector, we can create an observable called the *effective mass* [16]:

$$m_{\text{eff}} = p_{T,\text{jet1}} + p_{T,\text{jet2}} + p_{T,\text{jet3}} + p_{T,\text{jet4}} + \not{E}_{\mathrm{T}}, \tag{2.14}$$

where $p_T = \sqrt{p_x^2 + p_y^2}$ is the *transverse momentum*, and $\not{E}_{\mathrm{T}}$ is the *missing transverse energy*, defined as the momentum imbalance in the x, y plane due to the lightest neutralinos which escape detection. Here, the word *jet* refers to the way quarks are detected. Thus, Equation (2.14) defines the effective mass, m_{eff}, as the sum of the p_T of the four most energetic jets plus the missing energy. It is a measure of the squark, gluino, and lightest neutralino masses combined.

All of these physical observables can be used to make mass measurements of SUSY events at the LHC. In addition, depending on the particular SUSY model or other particle physics model which describes nature, there may be other decay chains which can be investigated using similar theoretical considerations. Now that we know of some signals we expect to see, we should investigate how we can construct such signals and measure them using LHC data.

3 SUBTRACTION TECHNIQUES*

SUSY models with R-parity force the lightest SUSY particle to be stable, fulfilling one of the requirements for it to be dark matter. However, there is a drastic experimental drawback to this scenario. In SUSY models with R-parity, every collision event which produces SUSY particles must produce them in pairs. As previously described, this is because every interaction must contain an even number of SUSY particles.

Thus, each SUSY event will have two decay chains of SUSY particles. If signals which look like SUSY events are seen at the LHC, experimentalists will try to examine the events in order to partially reconstruct those SUSY particle decay chains. The events are reconstructed from combining information from the detectable SM particles which are decay products of the SUSY decay chains. However, since SUSY events always have two SUSY decay chains, while reconstructing one chain, the other will always be a background. This is because we cannot know experimentally which detectable SM particles came from which SUSY decay chain. Combining information of decay products from different decay chains in an event results in *combinatoric* background.

On top of this, there are also huge backgrounds from SM processes which have much larger cross-sections. Most of these backgrounds can be managed effectively with the use of some event selection cuts. However, the SM cross-sections are so much larger than the SUSY cross-sections that there will always be some background remaining from SM processes. If a SM event looks like a SUSY event, then it will be treated in the same way; the attempt will be made to reconstruct a SUSY decay chain from the SM event. Of course, this results in more background noise to the signal we really want to reconstruct.

---

*Part of this section is reprinted with permission from "Determination of Nonuniversal Supergravity Models at the Large Hadron Collider" by B. Dutta, T. Kamon, A. Krislock, N. Kolev, and Y. Oh, 2010, Phys. Rev. D 82, 115009, Copyright 2010 by The American Physical Society and "Supersymmetry Signals of Supercritical String Cosmology at the Large Hadron Collider" by B. Dutta, A. Gurrola, T. Kamon, A. Krislock, A. B. Lahanas, *et al.*, 2009 Phys. Rev. D 79, 055002, Copyright 2009 by The American Physical Society.

In order to deal with these backgrounds, there are some powerful subtraction techniques which can be utilized. These subtraction techniques are all based upon the idea that we can use the data itself to partially model the background. The data is managed in one way to reconstruct the signal from an event, and it is managed in a different way to model the background from an event. These subtraction techniques do not allow us to fully reconstruct any particular event. However, with enough statistics, the background sample can be subtracted away from the signal sample for many events. When used properly, these subtraction techniques can eliminate large portions of the combinatoric background from a SUSY signal.

3.1 Opposite-Sign Minus Like-Sign

The Opposite-Sign Minus Like-Sign (OS−LS) subtraction technique utilizes the charges of lepton decay products to model and subtract the background. Consider the decay chain shown in Fig. 4. Due to conservation of charge in the decays, the two τ leptons have opposite charges.

In order to partially reconstruct this decay chain, information about the two τ leptons from this decay chain can be combined. However, experimentally, we cannot know which τ leptons come from this decay chain, and which τ leptons come from either the SUSY combinatoric background or the SM background. We therefore must select combinations of all Opposite-Sign (OS) pairs of τ leptons. Some OS τ pairs will come from this decay chain, while other OS τ pairs will be either SUSY combinatoric background or SM background. We combine information from each OS τ pair into some observable, take for example $m_{\tau\tau}^{[\mathrm{OS}]}$. We fill this value into an OS histogram, and repeat this process for all our events.

Luckily, there are no decay chains either in SUSY or in SM which can produce Like-Sign (LS) τ leptons. Thus, any LS τ pairs must be either SUSY combinatoric background or SM background. Therefore, we can use the LS τ pairs to model the background. Once again, we combine information from each LS τ pair into our

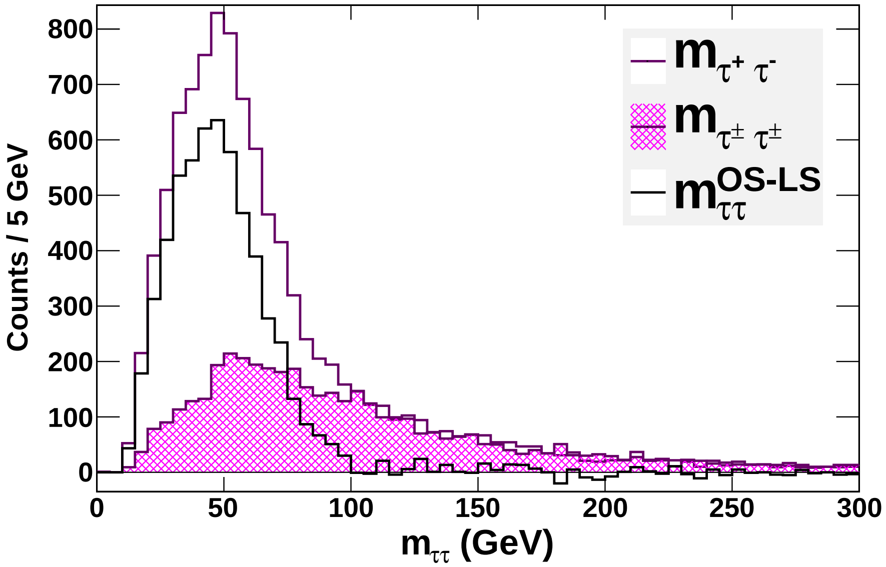

Figure 6: Ditau Invariant Mass. The two tau invariant mass distribution, $m_{\tau\tau}$ formed using SUSY collision events. This figure demonstrates the OS−LS subtraction technique. The OS and LS invariant mass distributions, $m_{\tau^+\tau^-}$ and $m_{\tau^\pm\tau^\pm}$, are shown as purple histograms, with the LS distribution filled with a hatch pattern. The resulting OS−LS subtraction leaves the black histogram, $m_{\tau\tau}^{\text{OS}-\text{LS}}$. The black histogram has most of the background removed, and we can resolve the endpoint, or maximum, of the $m_{\tau\tau}$ distribution.

observable $m_{\tau\tau}^{[\text{LS}]}$. We fill this value into a LS histogram for all our events as well.

Now our OS histogram contains the signal we want as well as the background. Our LS histogram models the background. Thus if we subtract the histograms (OS−LS), the resulting histogram of $m_{\tau\tau}^{[\text{OS}-\text{LS}]}$ has most of the background removed. In most cases, the endpoint $m_{\tau\tau}^{\text{max}}$ derived in Equation (2.10) can be measured from the OS−LS histogram. A demonstration of the OS−LS technique is shown for $m_{\tau\tau}$ in Figure 6.

This OS−LS technique is also useful in constructing the other physical observables for the decay chain shown in Figure 4. When constructing the physical observables to measure the endpoints $m_{J\tau}^{\text{max}}$ (Equation (2.11)) and $m_{J\tau\tau}^{\text{max}}$ (Equation (2.12)), we can select the OS and LS events in the same way. We pair up all tau leptons in the event. If a tau pair is OS, we use the tau leptons from that pair to calculate the invariant masses and fill the OS histograms. if a tau pair is LS, we do the same, but fill the LS histograms. Once again, the OS histograms will contain signal from the decay chain we want plus background. The LS histograms will contain only background. Thus, we again can subtract the histograms to remove background. This eliminates background even in the case of the jet tau invariant mass, $m_{J\tau}^{\max}$. Even though we use only the information from one of the two tau leptons in the pair for this observable, because we consider the pair as OS or LS before storing such information, the OS−LS subtraction will still isolate this particular decay chain from the background. Thus, this OS−LS technique is a very powerful means of removing the background for any observables which investigate these decay chains which involve taus or other leptons.

3.2 Bi-Event Subtraction Technique

This subtraction technique is another powerful means of modeling and removing vast amounts of combinatoric background. The premise is the same as the OS−LS technique: We wish to select from our data a sample which contains a useful signal and some background. We then select from our data another sample which contains only background which can be used to model the background in the former sample. Then we subtract to remove the background.

Consider again the decay chain shown in Figure 4. Suppose we are trying to construct the physical observable $m_{J\tau\tau}^{\max}$ from Equation (2.12). We should combine the tau leptons from this decay chain with the jet to form the invariant mass. However, as previously stated, every SUSY event has two SUSY decay chains in it. The other decay chain in the SUSY event will surely have another high-energy jet from a squark decay. The detector cannot really tell us which jet will make the correct combination.

To overcome this combinatoric background, we use another subtraction technique. We combine the tau pairs into OS and LS pairs as above. Then we combine these pairs with each of the two highest energy jets from the same event. Using each of these combinations, we form the invariant mass $m_{J\tau\tau}^{\text{same}}$ and fill the same event histogram. This histogram will be filled twice per every tau pair in each event. It will contain the correct combination of jet and tau leptons from the decay chain in Figure 4, as well as combinations of the wrong jet with the tau leptons.

Then, we take these same tau pairs and combine them with each of the two highest energy jets from a *different* event, which must pass the same event selection cuts as the current event. Using these new combinations, we form the invariant mass $m_{J\tau\tau}^{\text{bi}}$ and fill the *bi-event* histogram. This histogram will contain only wrong combinations, because there is no way for a jet from a different collision event to be part of the same decay chain as the tau leptons. Thus, we can use this bi-event histogram to model the background. Modeling the background with a bi-event histogram has been done before [17]. However, we generalize the technique here.

To perform the subtraction, first we perform the OS$-$LS subtraction as before. This will result in two remaining histograms: One which is OS$-$LS for the taus with a same-event jet, and one which is OS$-$LS for the taus with a bi-event jet. These two histograms are demonstrated in Figures 7 and 8. Each of these histograms should show no maximum, since there is no reason for a maximum to occur for invariant masses of the background jet and two tau combinations. Thus, we can normalize the shape of the bi-event histogram to the shape of the same-event histogram in the region of large $m_{J\tau\tau}$. Then, by subtracting the two histograms, same-event minus normalized bi-event, we remove a large amount of background. This is called the *Bi-Event Subtraction Technique* or BEST. The demonstration of the BEST is shown in Figure 9, which shows the subtraction between the $m_{J\tau\tau}^{\text{OS}-\text{LS, same}}$ distribution and the normalized $m_{J\tau\tau}^{\text{OS}-\text{LS, bi}}$ distribution.

This subtraction technique can be used for other endpoint measurements as well. For instance, in the same decay chain (Figure 4) our BEST can be used for the $m_{J\tau}$ endpoint measurement. Also, our BEST is especially powerful when it comes to decay chains involving W bosons, which need to be reconstructed from jets. Consider the decay chain shown in Figure 5. The W boson in this decay chain

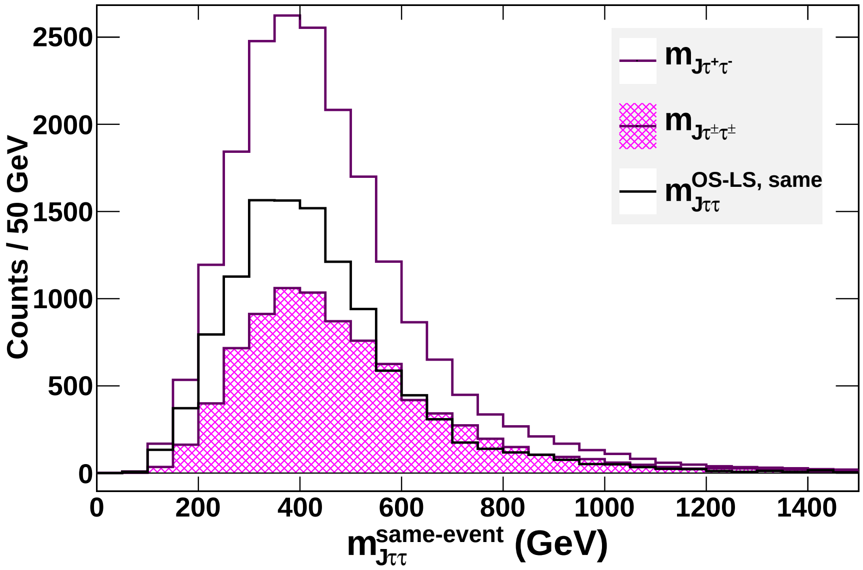

Figure 7: Jet-τ-τ Invariant Mass - Same. The jet plus two tau invariant mass distribution formed using jets in the *same event* as the taus, $m_{J\tau\tau}^{\text{same}}$ formed using SUSY collision events. This figure demonstrates the OS−LS subtraction technique. The OS and LS invariant mass distributions, $m_{J\tau^+\tau^-}$ and $m_{J\tau^\pm\tau^\pm}$, are shown as purple histograms, with the LS distribution filled with a hatch pattern. The resulting OS−LS subtraction leaves the black histogram, $m_{J\tau\tau}^{\text{OS−LS, same}}$. The black histogram has most of the background coming from the tau combinatoric background removed.

decays primarily into quark pairs which make two jets in the detector. These jets from the W boson decay are much less energetic than jets which come from the squark decays. Since the two highest energy jets are usually the ones from the squark decays, we ignore these jets while attempting to reconstruct W bosons. However, this leaves all the combinations of the lower energy jets for us to contend with.

Once again, we can use our BEST to deal with the combinatoric background. All pairs of low energy jets in an event are combined to form same-event invariant masses, m_{jj}^{same} which fill a same-event histogram. These same-event jet pairs may come from the W boson, or they may come from the combinatoric background. Next, we take each low energy jet from the current event is combined with a low energy jet from a different event, which again passes the same cuts as the current

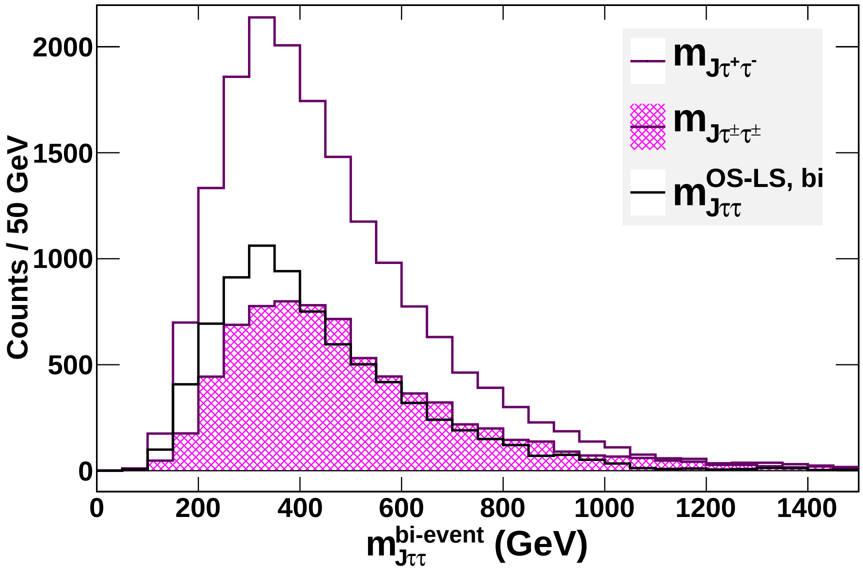

Figure 8: Jet-τ-τ Invariant Mass - Bi. The jet plus two tau invariant mass distribution formed using jets from a *different event* as the taus, $m^{\text{bi}}_{J\tau\tau}$ formed using SUSY collision events. This figure demonstrates the OS−LS subtraction technique. The OS and LS invariant mass distributions, $m_{J\tau^+\tau^-}$ and $m_{J\tau^\pm\tau^\pm}$, are shown as purple histograms, with the LS distribution filled with a hatch pattern. The resulting OS−LS subtraction leaves the black histogram, $m^{\text{OS−LS, bi}}_{J\tau\tau}$. The black histogram has most of the background coming from the tau combinatoric background removed.

event. These combinations form the bi-event invariant masses, m^{bi}_{jj}. None of these combinations can possibly come from a single W boson, and thus, they model the combinatoric background. We fill these invariant masses into the bi-event histogram. We can normalize the shape of the bi-event histogram to the shape of the same-event histogram in the region far away from the W boson mass, say $m_{jj} > 150$ GeV. Lastly, we subtract the two histograms, same-event minus bi-event, once again removing a large amount of the combinatoric background.

When we are finished with this BEST used to find the W bosons, we can select these W bosons using another subtraction technique which is described in the next subsection. Then, once we are done selecting these W bosons, we can *use our BEST again* to combine the W with the leading energy jets. This last BEST will remove a large proportion of combinatoric background associated with choosing the

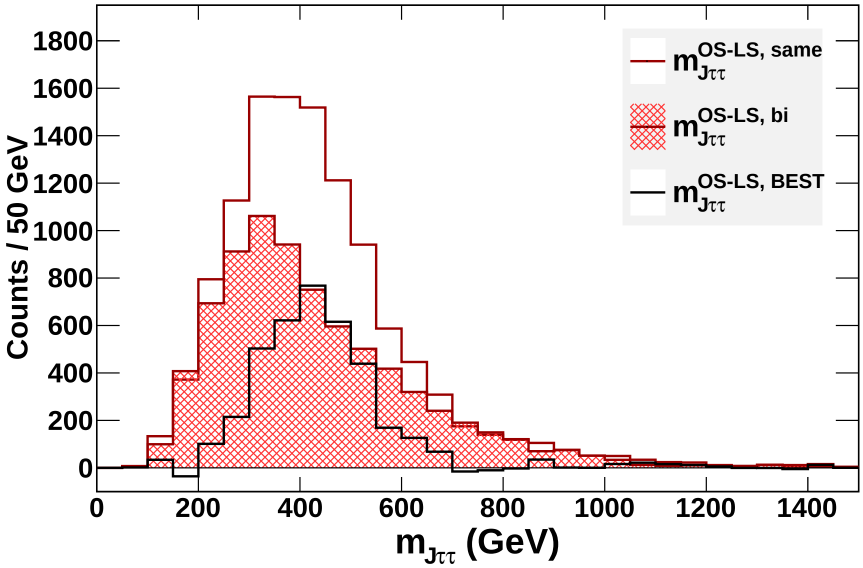

Figure 9: Jet-τ-τ Invariant Mass - BEST. The jet plus two tau invariant mass distribution formed using SUSY collision events. This figure demonstrates our BEST. The same-event and bi-event invariant mass distributions, $m_{J\tau\tau}^{\text{OS}-\text{LS, same}}$ and $m_{J\tau\tau}^{\text{OS}-\text{LS, bi}}$, are shown as red histograms, with the bi-event distribution filled with a hatch pattern. These distributions have already undergone the OS$-$LS subtraction which removed the tau combinatoric background. The bi-event histogram has been normalized to the shape of the same-event histogram in the high invariant mass region $m_{J\tau\tau} > 900$ GeV. The black distribution, $m_{J\tau\tau}^{\text{OS}-\text{LS, BEST}}$, is the resulting same-event minus bi-event subtraction, and has most of the remaining background coming from the jet combinatoric background removed. This distribution does not show a very nice endpoint. However, the peak position around $m_{J\tau\tau} \simeq 450$ GeV can also be measured.

correct leading jet from the decay chain.

3.3 Sideband Subtraction

The sideband subtraction is a means of removing combinatoric background as above. In particular, the sideband subtraction is used when the decay chain of interest has a particle which can be fully reconstructed. For example, consider the decay chain shown in Figure 10. In this decay chain, we would like to construct an

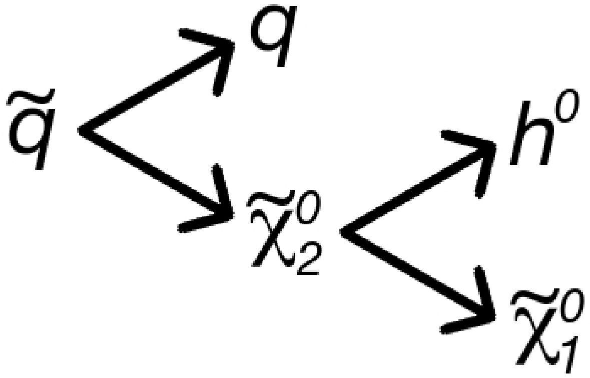

Figure 10: H-plus-Jet Decay Chain. SUSY decay chain. A squark decays into a quark and the second lightest neutralino. This neutralino then decays into the lightest neutralino and the lightest Higgs boson. The Higgs boson decays predominantly to b quarks, which can be identified uniquely as b jets in the detector.

observable out of the Higgs boson and leading jet.

In order to reconstruct the Higgs boson for use in this observable, we must fully reconstruct it from its decay products, which show up as two b jets in the detector. As usual, since we do not know which b jets come from the Higgs boson, and which come from other sources, we collect all pairs of b jets for events which pass our selection cuts. For each pair of b jets, we form the invariant mass m_{bb}, and fill a histogram. This histogram will show a peak around the Higgs boson mass, as well as some background signal. We can use the shape of this signal as a way to model the background. The b jet pairs which have invariant masses within the Higgs boson mass peak will consist of b jet pairs from the Higgs boson, as well as b jet pairs from the combinatoric background. We can model this combinatoric background by selecting b jet pairs which have invariant masses in the region away from the Higgs boson peak. We choose this region to be on either side of the Higgs mass region, and call it the *sideband* region. We show this graphically in Figure 11.

With these choices for regions, we can begin to form the invariant mass m_{Jbb} using a leading jet with our b pair. If the b pair is within the Higgs boson mass window, or $h$band, which is shown as a cyan filled region in Figure 11, we fill the $h$band

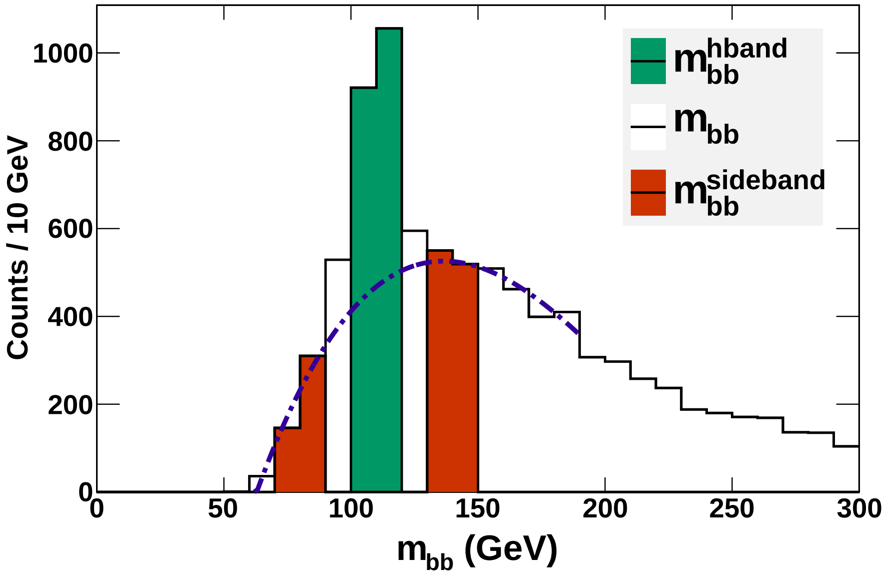

Figure 11: Di-b Invariant Mass. The b jet pair invariant mass, formed using SUSY events containing the decay chain shown in Figure 10. The green region is within the Higgs boson mass region, 100 GeV $\leq m_{bb} \leq$ 120 GeV. (The lightest Higgs boson has mass $m_h \simeq 114$ GeV for this model). The orange regions are the sideband regions, which contain only combinatoric background. A fit of the background signal, ignoring the Higgs boson mass peak, is shown as a dotted dashed purple line.

distribution, $m_{Jbb}^{h\text{band}}$. If, instead, the b pair is within one of the sidebands, shown as orange filled regions in Figure 11, we fill the sideband distribution, $m_{Jbb}^{\text{sideband}}$.

Next we fit the shape of the background region, ignoring the Higgs boson mass peak, in Figure 11. This background fit is shown as a purple dotted-dashed line. Using this background fit, we can normalize the sideband signal to the size of the background in the Higgs mass window which is implied by the background fit. This normalization is performed as follows. Let $f_{\text{BG}}(m_{bb})$ be the fit result of the background shape. Then we can calculate a normalization factor:

$$N_{bb}^{\text{sideband}} = \frac{\displaystyle\int_{100\text{ GeV}}^{120\text{ GeV}} f_{\text{BG}}(m_{bb})\text{d}m_{bb}}{\displaystyle\int_{70\text{ GeV}}^{90\text{ GeV}} f_{\text{BG}}(m_{bb})\text{d}m_{bb} + \int_{130\text{ GeV}}^{150\text{ GeV}} f_{\text{BG}}(m_{bb})\text{d}m_{bb}}, \tag{3.1}$$

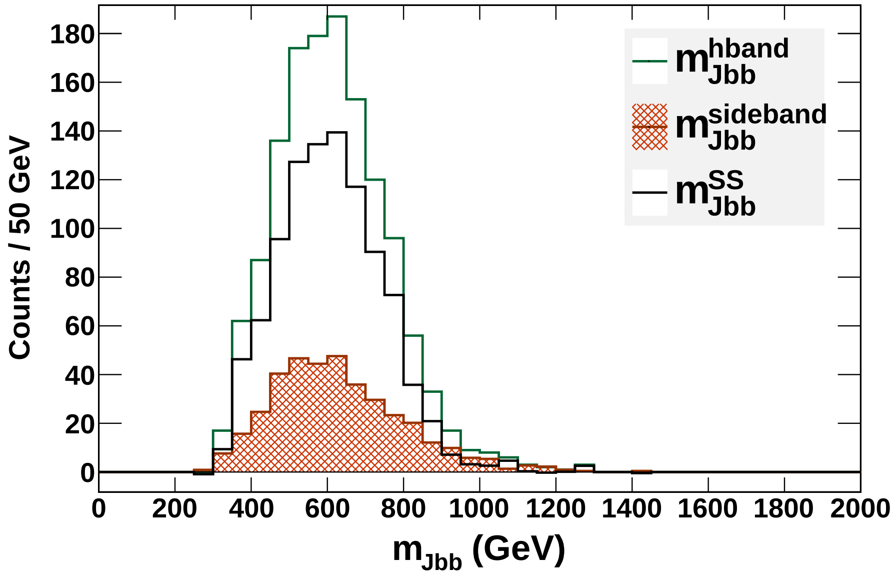

Figure 12: H-plus-Jet Invariant Mass. The jet plus Higgs invariant mass, formed using SUSY events containing the decay chain shown in Figure 10. The green histogram is formed using b jet pairs within the Higgs region of Figure 11. The dark orange, hatch filled histogram is formed using b jet pairs within the sideband regions of Figure 11, and is normalized using the normalization factor calculated from Equation (3.1). The subtraction of these two histograms, given by Equation (3.2) is the resulting black histogram. The black histogram shows a reduction in the background, and the endpoint of this histogram is clearly visible.

where the limits of integration relate to the sideband regions,
70 GeV $\leq m_{bb} \leq$ 90 GeV and 130 GeV $\leq m_{bb} \leq$ 150 GeV, and the $h$band region,
100 GeV $\leq m_{bb} \leq$ 120 GeV.

With the normalization factor calculated in Equation (3.1), we can perform the sideband subtraction. Using a leading h to denote the jet plus Higgs sideband distribution as $\mathrm{h}m_{Jbb}^{\mathrm{sideband}}$, and the jet plus Higgs $h$band distribution as $\mathrm{h}m_{Jbb}^{h\mathrm{band}}$, the sideband subtraction is

$$\mathrm{h}m_{Jbb}^{\mathrm{SS}} = \mathrm{h}m_{Jbb}^{h\mathrm{band}} - N_{bb}^{\mathrm{sideband}}\mathrm{h}m_{Jbb}^{\mathrm{sideband}}, \tag{3.2}$$

where SS denotes the completion of the sideband subtraction. After the subtraction is performed, a large amount of background, which consists of b jet pairs which are not both from a single Higgs boson decay, is removed. A sample sideband subtraction is shown in Figure 12.

3.4 BEST Plus Sideband Subtraction Examples

As an example, suppose we have a sample of events, some of which contain the SUSY decay chain shown in Figure 5. For all of these events we must prepare for the three subtractions which will remove great portions of the background. These three subtractions are the BEST which helps to find the W bosons from pairs of jets, the sideband subtraction which pins down the W bosons more precisely, and the final BEST which removes much of the remaining background associated with combining the W boson with the leading jets to form the final observable. To make the following discussions easier, we refer to the three subtractions as the W BEST, W sideband, and final BEST, respectively.

To prepare for these subtractions, we will need to set up a variety of histograms. All of these histograms will be necessary for the subtractions. We use the following notation to denote these histograms: A leading h denotes that we are referring to the histogram of invariant masses for all events, rather than just the invariant mass itself. A capital J in the subscript denotes a jet which is one of the two leading jets of its event, whereas a lower case j denotes a lower energy jet. An apostrophe, or prime symbol, following a jet denotes that the jet comes from a different event. For instance, j denotes a lower energy jet from the current event, whereas J' denotes one of the two leading energy jets from a different event. The superscript is reserved for describing the subtractions which will be, or have been performed, as well as whether or not the lower energy jet pair lies within the Wband or the sideband. With this notation, we describe the necessary histograms.

First, we will need the histograms to find the W bosons, perform the W BEST, and set up the W sideband subtraction. These histograms are hm_{jj}, and h$m_{jj'}$. Then we will need a total of eight histograms for the three subtractions needed for the m_{JW} signal. These histograms are h$m_{Jjj}^{W\text{band}}$, h$m_{Jjj'}^{W\text{band}}$, h$m_{J'jj}^{W\text{band}}$, h$m_{J'jj'}^{W\text{band}}$, h$m_{Jjj}^{\text{sideband}}$, h$m_{Jjj'}^{\text{sideband}}$, h$m_{J'jj}^{\text{sideband}}$, and h$m_{J'jj'}^{\text{sideband}}$. Finally, for the purposes of this explanation, it is less confusing to have additional histograms to contain each subtraction. The first subtraction is the BEST for finding W bosons, with histograms hm_{jj}^{BEST}, h$m_{Jjj}^{W\text{band, BEST}}$, h$m_{Jjj}^{\text{sideband, BEST}}$, h$m_{J'jj}^{W\text{band, BEST}}$, and h$m_{J'jj}^{\text{sideband, BEST}}$. The next subtraction to be performed is the sideband subtraction (SS), resulting in histograms h$m_{Jjj}^{\text{SS, BEST}}$ and h$m_{J'jj}^{\text{SS, BEST}}$. The final subtraction is the BEST which removes some background for the leading jets, leading to the final histogram hm_{Jjj}^{FINAL}.

With all of these histograms created, next we loop over our entire event sample. For every event which passes our event selection cuts, we do the following: We store the jet information for the entire event, so that this event can be used as a bi-event for the next event which passes selection cuts. We loop over all pairs of low energy jets in the event and form the invariant mass m_{jj} which fills our hm_{jj} histogram. If m_{jj} falls within the Wband, where 65 GeV $\leq m_{jj} \leq$ 90 GeV, we combine this jet pair with each of the two leading energy jets to form two m_{Jjj} values. Both of these values fill the h$m_{Jjj}^{W\text{band}}$ histogram, which means there are two entries for this low energy jet pair. If, instead, m_{jj} falls within the sidebands, where 40 GeV $\leq m_{jj} \leq$ 55 GeV or 100 GeV $\leq m_{jj} \leq$ 115 GeV, we still combine with the leading jets to form two m_{Jjj} values. However, for this case we fill the h$m_{Jjj}^{\text{sideband}}$ histogram with these values. For all events except the first which pass the cuts, we also form the invariant mass for all combinations of low energy jets with the leading jets from the previous event to form $m_{J'jj}$ values. As before, we sort these values into the h$m_{J'jj}^{W\text{band}}$ and h$m_{J'jj}^{\text{sideband}}$ histograms depending on the value of m_{jj}. Lastly, we repeat this entire process for the case of one low energy jet from this event and one from the previous event forming the invariant masses $m_{jj'}$ which fills the h$m_{jj'}$ histogram. We consider this bi-event low energy jet pair in just the same way as the same-event pair before, forming the additional invariant masses $m_{Jjj'}$ and $m_{J'jj'}$. Again, we sort the bi-event jet pairs into Wband and sideband to fill the histograms h$m_{Jjj'}^{W\text{band}}$, h$m_{Jjj'}^{\text{sideband}}$, h$m_{J'jj'}^{W\text{band}}$, and h$m_{J'jj'}^{\text{sideband}}$.

Once we have done this for all of our events, we can begin to perform the

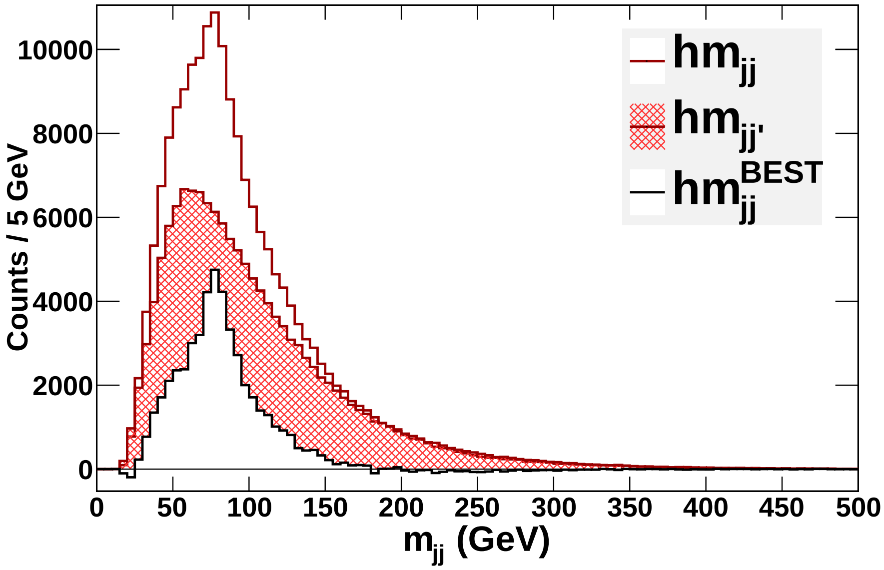

Figure 13: Dijet Invariant Mass. The two jet invariant mass distribution used to find W bosons formed using SUSY collision events. This figure demonstrates our BEST. The same-event and bi-event invariant mass distributions, $\mathrm{h}m_{jj}$ and $\mathrm{h}m_{jj'}$, are shown as red histograms, with the bi-event distribution filled with a hatch pattern. The bi-event histogram has been normalized to the shape of the same-event histogram in the high invariant mass region $m_{jj} > 150$ GeV, using the normalization factor calculated in Equation (3.3). The black distribution, m_{jj}^{BEST}, is the resulting same-event minus bi-event subtraction given by Equation (3.4a), and has most of the remaining background coming from the jet combinatoric background removed. We can clearly see in this figure a drastic reduction of the background which obscures the W boson mass peak around $m_{jj} \simeq 80$ GeV.

subtractions. We start with the first BEST based on the $\mathrm{h}m_{jj}$ and $\mathrm{h}m_{jj'}$ distributions. First we calculate a normalization factor. Considering the histograms as a function of the invariant mass, i.e. $\mathrm{h}m_{jj}(m_{jj})$, this normalization factor can be written as

$$N_{jj}^{\mathrm{BEST}} = \frac{\displaystyle\int_{150\ \mathrm{GeV}}^{500\ \mathrm{GeV}} \mathrm{h}m_{jj}(m_{jj})\mathrm{d}m_{jj}}{\displaystyle\int_{150\ \mathrm{GeV}}^{500\ \mathrm{GeV}} \mathrm{h}m_{jj'}(m_{jj'})\mathrm{d}m_{jj'}}, \tag{3.3}$$

where the lower limit of integration is chosen to be greater than both the Wband and sideband regions, and the upper limit of integration is chosen large as though

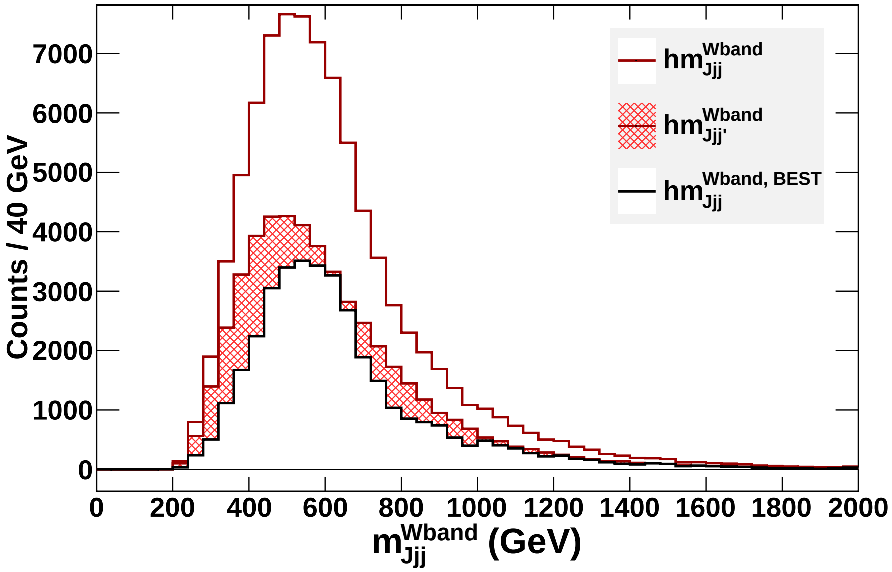

Figure 14: Trijet Invariant Mass - Same - Wband. The three jet invariant mass distribution $\mathrm{h}m_{Jjj}^{W\mathrm{band}}$ showing the BEST which removes the combinatoric background of soft jets for the W boson reconstruction. The same-event and bi-event invariant mass distributions, $\mathrm{h}m_{Jjj}^{W\mathrm{band}}$ and $\mathrm{h}m_{Jjj'}^{W\mathrm{band}}$, are shown as red histograms, with the bi-event distribution filled with a hatch pattern. The bi-event histogram has been normalized using the normalization factor calculated in Equation (3.3). The black distribution, $\mathrm{h}m_{Jjj}^{W\mathrm{band,\ BEST}}$, is the resulting same-event minus bi-event subtraction given by Equation (3.4b).

we are integrating to infinity. With this normalization factor, we can perform the first BEST subtraction for our histograms:

$$\mathrm{h}m_{jj}^{\mathrm{BEST}} = \mathrm{h}m_{jj} - N_{jj}^{\mathrm{BEST}}\mathrm{h}m_{jj'} \tag{3.4a}$$

$$\mathrm{h}m_{Jjj}^{W\mathrm{band,\ BEST}} = \mathrm{h}m_{Jjj}^{W\mathrm{band}} - N_{jj}^{\mathrm{BEST}}\mathrm{h}m_{Jjj'}^{W\mathrm{band}} \tag{3.4b}$$

$$\mathrm{h}m_{Jjj}^{\mathrm{sideband,\ BEST}} = \mathrm{h}m_{Jjj}^{\mathrm{sideband}} - N_{jj}^{\mathrm{BEST}}\mathrm{h}m_{Jjj'}^{\mathrm{sideband}} \tag{3.4c}$$

$$\mathrm{h}m_{J'jj}^{W\mathrm{band,\ BEST}} = \mathrm{h}m_{J'jj}^{W\mathrm{band}} - N_{jj}^{\mathrm{BEST}}\mathrm{h}m_{J'jj'}^{W\mathrm{band}} \tag{3.4d}$$

$$\mathrm{h}m_{J'jj}^{\mathrm{sideband,\ BEST}} = \mathrm{h}m_{J'jj}^{\mathrm{sideband}} - N_{jj}^{\mathrm{BEST}}\mathrm{h}m_{J'jj'}^{\mathrm{sideband}} \tag{3.4e}$$

These subtractions are all demonstrated. See Figures 13, 14, 15, 16, and 17.

With the first application of our BEST finished, we can prepare for the sideband

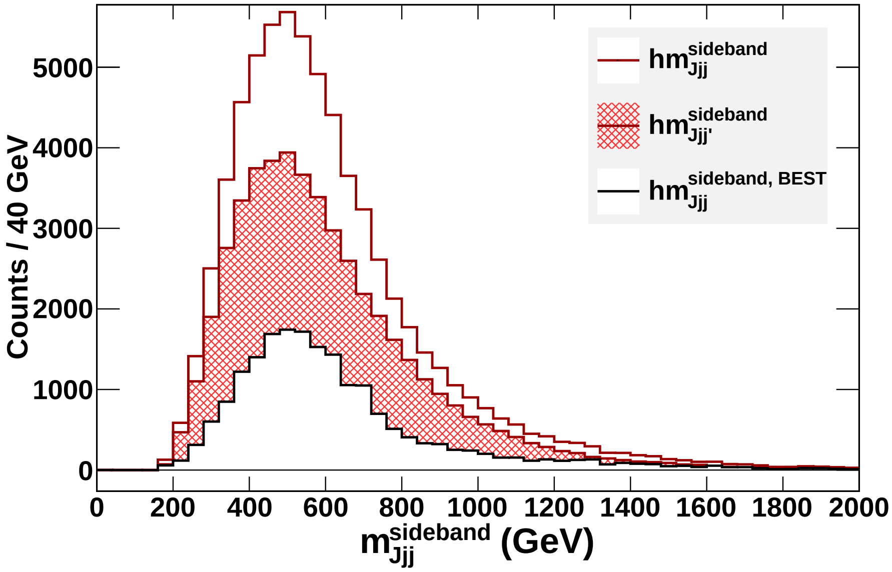

Figure 15: Trijet Invariant Mass - Same - Sideband. The three jet invariant mass distribution $hm_{Jjj}^{\text{sideband}}$ showing the BEST which removes the combinatoric background of soft jets for the W boson reconstruction. The same-event and bi-event invariant mass distributions, $hm_{Jjj}^{\text{sideband}}$ and $hm_{Jjj'}^{\text{sideband}}$, are shown as red histograms, with the bi-event distribution filled with a hatch pattern. The bi-event histogram has been normalized using the normalization factor calculated in Equation (3.3). The black distribution, $hm_{Jjj}^{\text{sideband, BEST}}$, is the resulting same-event minus bi-event subtraction given by Equation (3.4c).

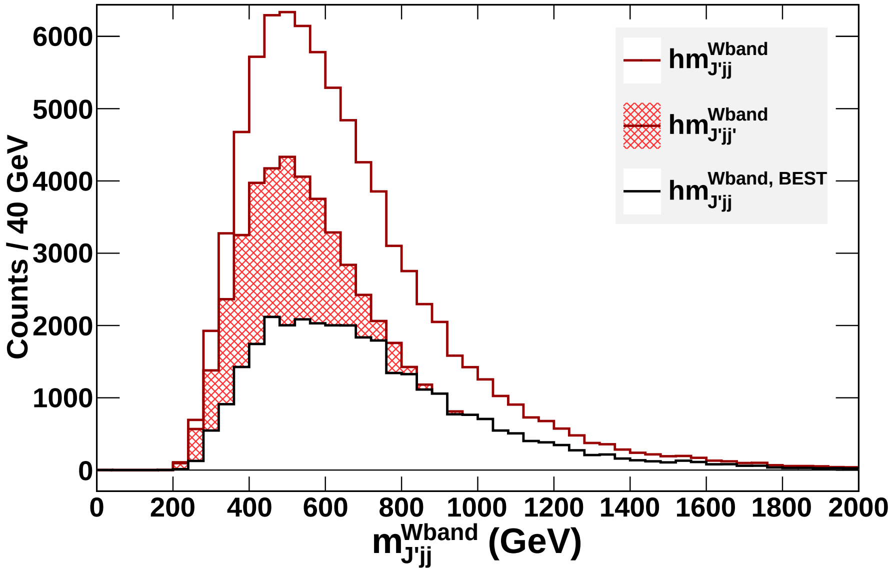

Figure 16: Trijet Invariant Mass - Bi - Wband. The three jet invariant mass distribution h$m_{J'jj}^{W\text{band}}$ showing the BEST which removes the combinatoric background of soft jets for the W boson reconstruction. The same-event and bi-event invariant mass distributions, h$m_{J'jj}^{W\text{band}}$ and h$m_{J'jj'}^{W\text{band}}$, are shown as red histograms, with the bi-event distribution filled with a hatch pattern. The bi-event histogram has been normalized using the normalization factor calculated in Equation (3.3). The black distribution, h$m_{J'jj}^{W\text{band, BEST}}$, is the resulting same-event minus bi-event subtraction given by Equation (3.4d).

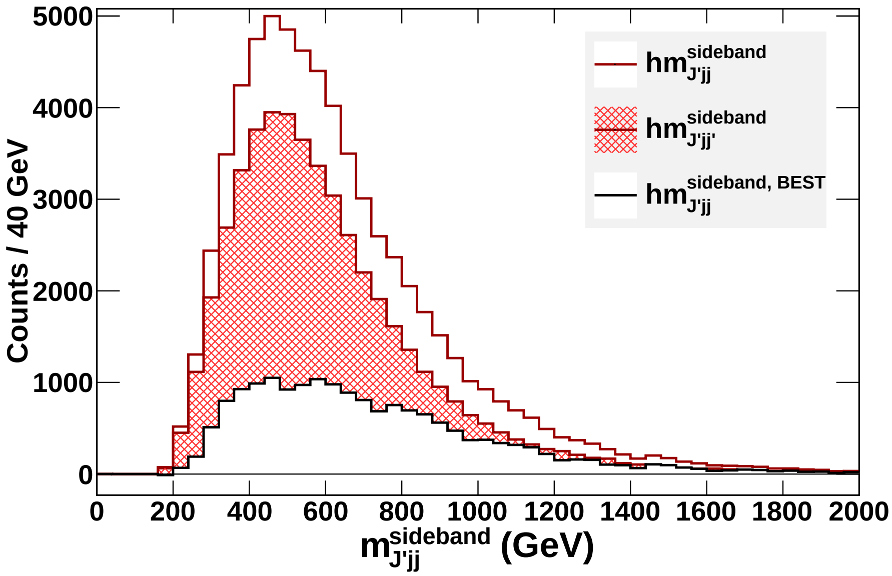

Figure 17: Trijet Invariant Mass - Bi - Sideband. The three jet invariant mass distribution $\mathrm{h}m_{J'jj}^{\mathrm{sideband}}$ showing the BEST which removes the combinatoric background of soft jets for the W boson reconstruction. The same-event and bi-event invariant mass distributions, $\mathrm{h}m_{J'jj}^{\mathrm{sideband}}$ and $\mathrm{h}m_{J'jj'}^{\mathrm{sideband}}$, are shown as red histograms, with the bi-event distribution filled with a hatch pattern. The bi-event histogram has been normalized using the normalization factor calculated in Equation (3.3). The black distribution, $\mathrm{h}m_{J'jj}^{\mathrm{sideband,\ BEST}}$, is the resulting same-event minus bi-event subtraction given by Equation (3.4e).

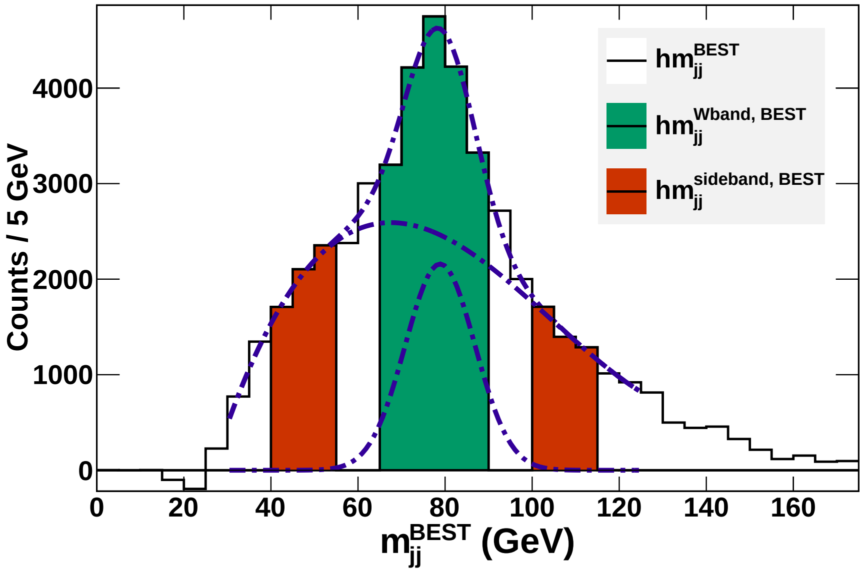

Figure 18: Dijet Invariant Mass - Regions. The jet pair invariant mass, formed using SUSY events containing the decay chain shown in Figure 5. This histogram is already the result of the BEST performed in Equation (3.4a). The green region is within the W boson mass region, 65 GeV $\leq m_{jj} \leq$ 90 GeV. (The W boson has mass $m_W \simeq$ 80 GeV). The orange regions are the sideband regions, 40 GeV $\leq m_{jj} \leq$ 55 GeV and 100 GeV $\leq m_{jj} \leq$ 115 GeV, which contain only combinatoric background. A fit of the W boson signal as well as the background, is shown as a dotted dashed purple line. The fit is broken down into the W signal component (a bell curve) and a background component (a cubic polynomial) in the figure as well.

subtraction. First, we fit the shape of the hm_{jj}^{BEST} distribution. We choose a fit function that is a combination of two shapes. One shape will fit the W mass peak, which should be a gaussian bell curve shape. The other shape should fit the background. We can choose whatever shape seems to fit the background well, at lease in the region which covers the sidebands and the Wband. Thus, we should choose a shape which fits the background well in the region 40 GeV $\leq m_{jj} \leq$ 115 GeV. For this demonstration, we choose a cubic polynomial to fit the shape of the background. The plot of the hm_{jj}^{BEST} distribution, showing the Wband, sidebands, and the fit is shown in Figure 18.

Taking the background region fit result, $g_{\mathrm{BG}}(m_{jj}^{\mathrm{BEST}})$, we can determine the

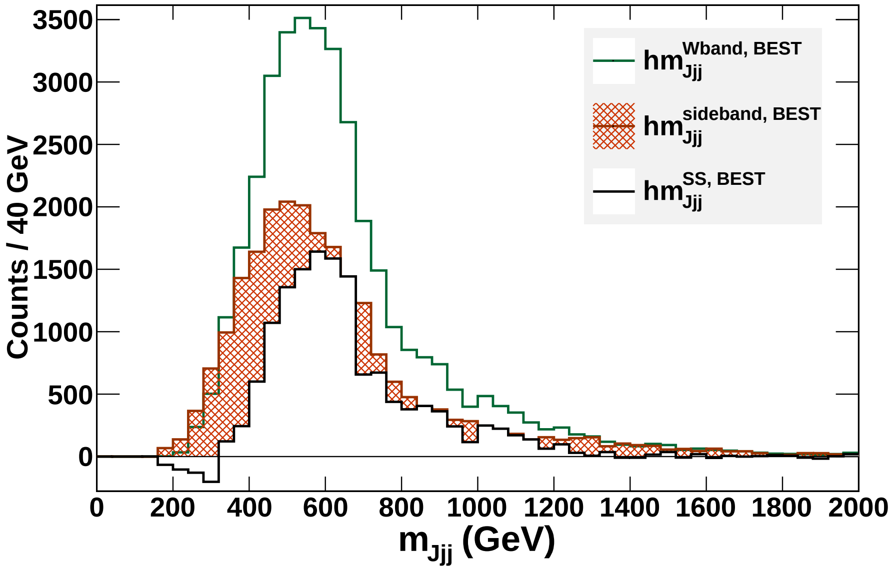

Figure 19: Trijet Invariant Mass - Same - Sideband Subtracted. The three jet invariant mass distribution $\mathrm{h}m_{Jjj}^{\mathrm{BEST}}$ showing the sideband subtraction which removes most of the remaining combinatoric background of soft jets for the W boson reconstruction. The Wband and sideband invariant mass distributions, $\mathrm{h}m_{Jjj}^{W\text{band, BEST}}$ and $\mathrm{h}m_{Jjj}^{\text{sideband, BEST}}$, are shown as green and orange histograms respectively, with the sideband distribution filled with a hatch pattern. The sideband histogram has been normalized using the normalization factor calculated in Equation (3.5). The black distribution, $\mathrm{h}m_{Jjj}^{\text{SS, BEST}}$, is the resulting Wband minus sideband subtraction given by Equation (3.6a), and has most of the remaining background coming from the jet combinatoric background of soft jets removed.

sideband normalization factor in the same way as Equation (3.1):

$$N_{jj}^{\text{sideband}} = \frac{\displaystyle\int_{65\text{ GeV}}^{90\text{ GeV}} g_{\mathrm{BG}}(m_{jj}^{\mathrm{BEST}})\mathrm{d}m_{jj}^{\mathrm{BEST}}}{\displaystyle\int_{40\text{ GeV}}^{55\text{ GeV}} g_{\mathrm{BG}}(m_{jj}^{\mathrm{BEST}})\mathrm{d}m_{jj}^{\mathrm{BEST}} + \int_{100\text{ GeV}}^{115\text{ GeV}} g_{\mathrm{BG}}(m_{jj}^{\mathrm{BEST}})\mathrm{d}m_{jj}^{\mathrm{BEST}}}, \tag{3.5}$$

With this normalization factor, we perform the sideband subtraction for our

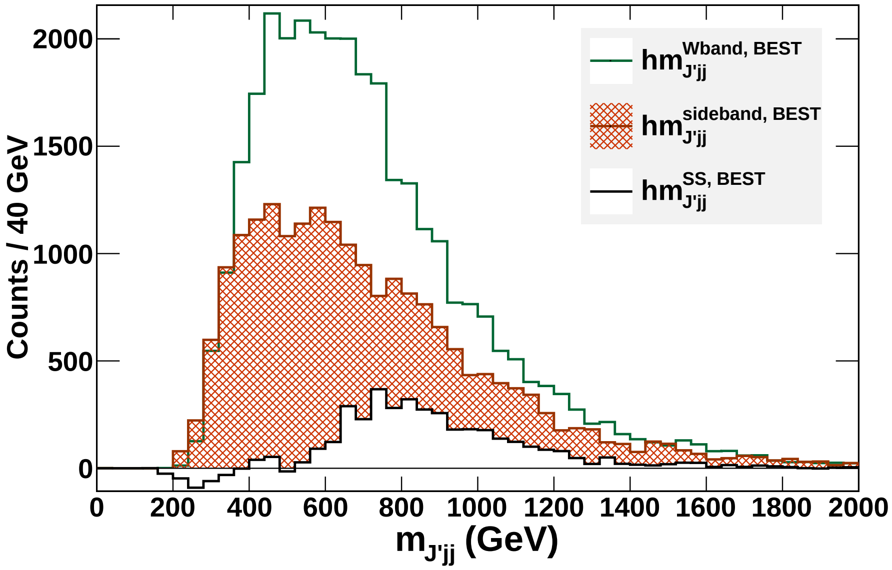

Figure 20: Trijet Invariant Mass - Same - Sideband Subtracted. The three jet invariant mass distribution $\mathrm{h}m_{J'jj}^{\mathrm{BEST}}$ showing the sideband subtraction which removes most of the remaining combinatoric background of soft jets for the W boson reconstruction. The Wband and sideband invariant mass distributions, $\mathrm{h}m_{J'jj}^{W\mathrm{band,\ BEST}}$ and $\mathrm{h}m_{J'jj}^{\mathrm{sideband,\ BEST}}$, are shown as green and orange histograms respectively, with the sideband distribution filled with a hatch pattern. The sideband histogram has been normalized using the normalization factor calculated in Equation (3.5). The black distribution, $\mathrm{h}m_{J'jj}^{\mathrm{SS,\ BEST}}$, is the resulting Wband minus sideband subtraction given by Equation (3.6b), and has most of the remaining background coming from the jet combinatoric background of soft jets removed.

remaining histograms:

$$\mathrm{h}m_{Jjj}^{\mathrm{SS,\ BEST}} = \mathrm{h}m_{Jjj}^{W\mathrm{band,\ BEST}} - N_{jj}^{\mathrm{sideband}}\mathrm{h}m_{Jjj}^{\mathrm{sideband,\ BEST}} \tag{3.6a}$$

$$\mathrm{h}m_{J'jj}^{\mathrm{SS,\ BEST}} = \mathrm{h}m_{J'jj}^{W\mathrm{band,\ BEST}} - N_{jj}^{\mathrm{sideband}}\mathrm{h}m_{J'jj}^{\mathrm{sideband,\ BEST}} \tag{3.6b}$$

These subtractions are also demonstrated. See Figures 19, and 20.

Finally, we can perform the remaining BEST to remove the combinatoric background from the leading jets in the event. We calculate the normalization factor just as we did before in Equation (3.3). Again, we consider our last two histograms as a function of the invariant mass: $\mathrm{h}m_{Jjj}^{\mathrm{SS,\ BEST}}(m_{Jjj})$ and

$\mathrm{h}m_{J'jj}^{\text{SS, BEST}}(m_{J'jj})$. However, for the calculation of this normalization factor, we need a little more care. The range we choose for the normalization factor calculation could effect our result. Experimentally, we don't have a point of reference for the normalization factor like we did for the W boson reconstruction. Before, we knew the W boson mass, and so we knew to stay away from that region. However, in this case we do not know for sure where the endpoint of the distribution will be. Thus, we should choose a normalization range as far in the tail region of the distribution as possible. The ideal normalization range is one which seems to match the background well without being too close to the endpoint. For this example demonstration, we choose the normalization range to be $1000\text{ GeV} \leq m_{Jjj} \leq 2000\text{ GeV}$.

Thus, the normalization factor chosen for this example demonstration is

$$N_{Jjj}^{\text{BEST}} = \frac{\displaystyle\int_{1000\text{ GeV}}^{2000\text{ GeV}} \mathrm{h}m_{Jjj}^{\text{SS, BEST}}(m_{Jjj})\mathrm{d}m_{Jjj}}{\displaystyle\int_{1000\text{ GeV}}^{2000\text{ GeV}} \mathrm{h}m_{J'jj}^{\text{SS, BEST}}(m_{J'jj})\mathrm{d}m_{J'jj}}. \tag{3.7}$$

Using this normalization factor, we can perform the final subtraction,

$$\mathrm{h}m_{Jjj}^{\text{FINAL}} = \mathrm{h}m_{Jjj}^{\text{SS, BEST}} - N_{Jjj}^{\text{BEST}}\mathrm{h}m_{J'jj}^{\text{SS, BEST}}, \tag{3.8}$$

which is demonstrated in Figure 21. Note in that figure that the endpoint shows clearly over the remaining background, at around $m_{Jjj} \simeq 800$ GeV. The normalization range we chose caused our BEST to perform wonderfully. The background is modeled well and subtracted away, and the normalization range is enough away from the resulting endpoint to give us confidence that we have not obscured the endpoint measurement. This is the power of our BEST.

To show off the power of BEST even more, we use it to reconstruct top quarks for $t\bar{t}$ events at a center of mass collision energy of $\sqrt{s} = 7$ TeV at the LHC. We generate hard scattering collision events using ALPGEN [18], perform the cascade decays with PYTHIA [11], and perform a LHC detector simulation using PGS4 [12]. The W+jets events are the main source of background for finding the

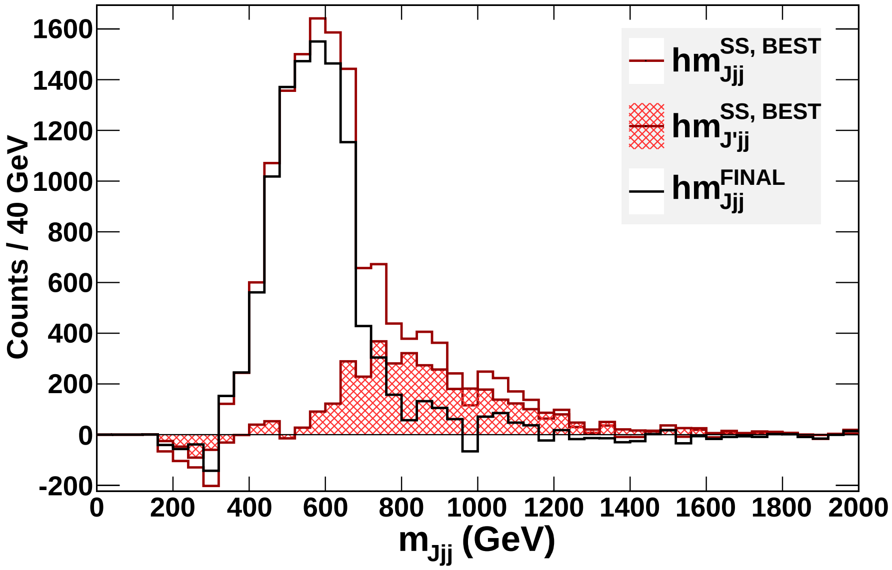

Figure 21: Trijet Invariant Mass - Final. The three jet invariant mass distribution $\mathrm{h}m_{Jjj}$ showing the final result of all subtractions. The last BEST removes most of the remaining combinatoric background from the leading jets. The same-event and bi-event invariant mass distributions, $\mathrm{h}m_{Jjj}^{\text{SS, BEST}}$ and $\mathrm{h}m_{J'jj}^{\text{SS, BEST}}$, are shown as red histograms, with the bi-event distribution filled with a hatch pattern. The bi-event histogram has been normalized using the normalization factor calculated in Equation (3.7). The black distribution, $\mathrm{h}m_{Jjj}^{\text{FINAL}}$, is the resulting same-event minus bi-event subtraction given by Equation (3.8), and has most of the remaining background coming from the jet combinatoric background of leading jets removed. The endpoint of the distribution, which is around $m_{Jjj} \simeq 800$ GeV, is clearly visible after this final application of our BEST.

top quark, so we generate these events in the same way. This background is mixed in randomly, according to production cross-sections, with our $t\bar{t}$ events. After PGS4 is finished with these events, we select events for analysis with the following cuts [19]: (a) Number of leptons, $N_\ell = 1$, where $p_T^{(\ell)} \geq 20$ GeV and $p_{T,iso}^{(\ell)} \leq 0.1 \times p_T^{(\ell)}$; (b) Missing transverse energy, $\not{E}_{\mathrm{T}} \geq 20$ GeV; (c) Number of jets, $N_j \geq 3$, where $p_T^{(j)} \geq 30$ GeV and at least one jet has been tightly b-tagged [12]; (d) Number of taus, $N_\tau = 0$ for taus with $p_T^{(\tau)} \geq 20$ GeV [12].

Selecting events in this way, we construct the trijet invariant mass distribution, $\mathrm{h}m_{bjj}^{\text{FINAL}}$. This distribution is generated exactly as described above, with the

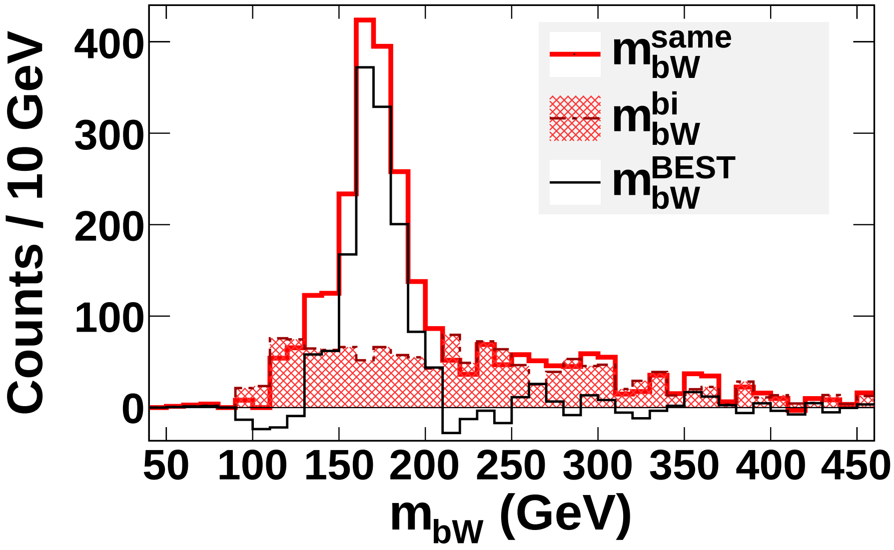

Figure 22: Top Reconstruction with BEST. The three jet invariant mass distribution hm_{bjj} showing the final result of all subtractions. BEST removes most of the combinatoric background, leaving a very clean top mass distribution. Performing a gaussian fit of this distribution yields a top mass of $m_t = 170.5 \pm 1.5$ GeV for an integrated luminosity of 2 fb^{-1}. The top quark mass is set within ALPGEN as $m_t = 174.3$ GeV.

exception that instead of using a leading jet, we use a *b*-tagged jet. Also, we consider all regular jets when constructing jet pairs as W boson candidates. The result of such an analysis shows a very nice top quark mass peak. This plot is shown in Figure 22. This example shows the power of BEST even in the midst of background events. Another example of this is shown in Section 4.4.

4 mSUGRA MOTIVATED MODELS STUDIED*

With all of these physical observables and measurement techniques, we can see how SUSY models may be probed at the LHC. Here, we examine some simple, well-motivated SUSY models which predict the correct amount of dark matter in the universe today. However, we stress that the observables and measurement techniques employed are very general and can be used for searches of many other models beyond the SM.

The starting point of all the models we examine here is the mSUGRA model. We choose it for its simplicity in having only four parameters and a sign to determine all the SUSY particle masses. We consider regions of parameter space within the mSUGRA model which have the correct amount of dark matter in the universe today [20]. We examine these models using our LHC simulation tools ISAJET, PYTHIA, and PGS4 [10, 11, 12] to see what the physical observables are which we can measure for this model point. We then use ROOT [13] as an analysis tool for the simulated data.

Using ROOT, we can create all the histograms, perform all the subtractions, and find the endpoints or peaks of our physical observables. We perform enough simulations in order to determine the behavior of the physical observables as a function of the model parameters. Once these *functional forms* are determined, we can find ways of inverting them so that we have the model parameters as a function of the physical observables. Taking the results of our simulations, we can see how well the LHC can determine the location of a particular model point in parameter space.

---

*Part of this section is reprinted with permission from "Determination of Nonuniversal Supergravity Models at the Large Hadron Collider" by B. Dutta, T. Kamon, A. Krislock, N. Kolev, and Y. Oh, 2010, Phys. Rev. D 82, 115009, Copyright 2010 by The American Physical Society, "Supersymmetry Signals of Supercritical String Cosmology at the Large Hadron Collider" by B. Dutta, A. Gurrola, T. Kamon, A. Krislock, A. B. Lahanas, *et al.*., 2009 Phys. Rev. D 79, 055002, Copyright 2009 by The American Physical Society, and "Determining the Dark Matter Relic Density in the Minimal Supergravity Stau-Neutralino Coannihilation Region at the Large Hadron Collider" by R. Arnowitt, B. Dutta, A. Gurrola, T. Kamon, A. Krislock, *et al.*., 2008 Phys. Rev. Lett. 100, 231802, Copyright 2008 by The American Physical Society.

Finally, we can use DARKSUSY [14] to calculate the dark matter relic density of the universe using the model paramters we found as a result of our LHC simulation. This determines how well the LHC can measure the dark matter relic density of the universe. We can compare the result from the LHC simulation to that of WMAP [1]. That is to say, the LHC can be an *independent measure* of the dark matter content of the universe from WMAP. This is one of our key goals for this analysis.

4.1 Co-annihilation Region

The *stau co-annihilation region* is one region within the mSUGRA model which predicts the correct amount of dark matter in the universe. The mechanism by which this region predicts the correct amount of dark matter in the universe is the annihilation between the stau, $\widetilde{\tau}$, and the lightest neutralino, $\widetilde{\chi}_1^0$. The annihilation between the stau and neutralino is referred to as *co-annihilation*, and it occurs when the stau is very close in mass with the neutralino [21]. This near mass degeneracy between the neutralino and stau is a smoking gun signal at the LHC [22, 23].

The co-annihilation signal at the LHC is characterized by the Jet-τ-τ decay chain, $\widetilde{q}_L \to q\widetilde{\chi}_2^0 \to q\tau\widetilde{\tau}_1 \to q\tau\tau\widetilde{\chi}_1^0$, which is shown in Figure 4. This decay chain causes events which have high energy jets (from decays of the squarks), low energy tau leptons (from the stau decaying into the neutralino), and missing energy (from the neutralino which escapes the detector). To make measurements of the SUSY particles in this decay chain, we employ the endpoint calculations of Section 2. In particular, we can use the endpoints $m_{\tau\tau}^{\max}$, $m_{J\tau}^{\max}$, and $m_{J\tau\tau}^{\max}$ as our physical observables. These endpoints have been determined in Equations (2.10), (2.11), and (2.12), respectively.

Using these observables together, the SUSY masses (or at least the mass differences) of the Jet-τ-τ decay chain can be measured. If we find a small mass difference $\Delta M \equiv m_{\widetilde{\tau}_1} - m_{\widetilde{\chi}_1^0}$, this is a smoking gun signal for the co-annihilation region of mSUGRA. Once we find this small mass difference, we can use some more

Table 3: Co-annihilation SUSY Mass Spectrum. SUSY particle masses (in GeV) for the co-annihilation region benchmark point: $m_0 = 210$ GeV, $m_{1/2} = 350$ GeV, $\tan\beta = 40$, $A_0 = 0$, and $\mu > 0$. Also shown is the mass difference $\Delta M \equiv m_{\widetilde{\tau}_1} - m_{\widetilde{\chi}_1^0}$.

$\widetilde{g}$	$\widetilde{u}_L$	$\widetilde{t}_2$	$\widetilde{b}_2$	$\widetilde{e}_L$	$\widetilde{\tau}_2$	$\widetilde{\chi}_2^0$	ΔM
	$\widetilde{u}_R$	$\widetilde{t}_1$	$\widetilde{b}_1$	$\widetilde{e}_R$	$\widetilde{\tau}_1$	$\widetilde{\chi}_1^0$	
831	748	728	705	319	329	260.3	10.6
	725	561	645	251	151.3	140.7	

physical observables to check the mSUGRA unification behavior. Then, if that check is successful, we can use the model itself to fully reconstruct the model parameters.

To demonstrate this, we start with a benchmark point which predicts roughly the correct abundance of dark matter. This benchmark point is chosen as $m_0 = 210$ GeV, $m_{1/2} = 350$ GeV, $\tan\beta = 40$, $A_0 = 0$, and $\mu > 0$. The mass spectrum and stau-neutralino mass difference for this benchmark point are shown in Table 3. We also vary each model parameter independently around the benchmark point. We do this so that we can see the behavior of each physical observable as a function of the SUSY masses, or as a function of the model parameters themselves. We perform a simulation of the LHC experiment for each of these model points.

Looking at the event sample for each simulation, we perform the partial reconstruction of the Jet-τ-τ decay chain. We construct the observables $m_{\tau\tau}$, $m_{J\tau}$, and $m_{J\tau\tau}$. Because the mass difference ΔM is small, there is an additional physical observable involving the lowest p_T tau lepton from the Jet-τ-τ decay chain. We construct this observable as well.

To construct these observables, we first use some selection cuts to choose a sample of events which has an abundance of this decay chain. These selection cuts also remove background from the SM. The primary SM backgrounds for this signal are $t\bar{t}$, W+Jets, and Z+Jets production. We select events which satisfy the following cuts: (a) Number of tau leptons in the event, $N_\tau \geq 2$ (for tau leptons with

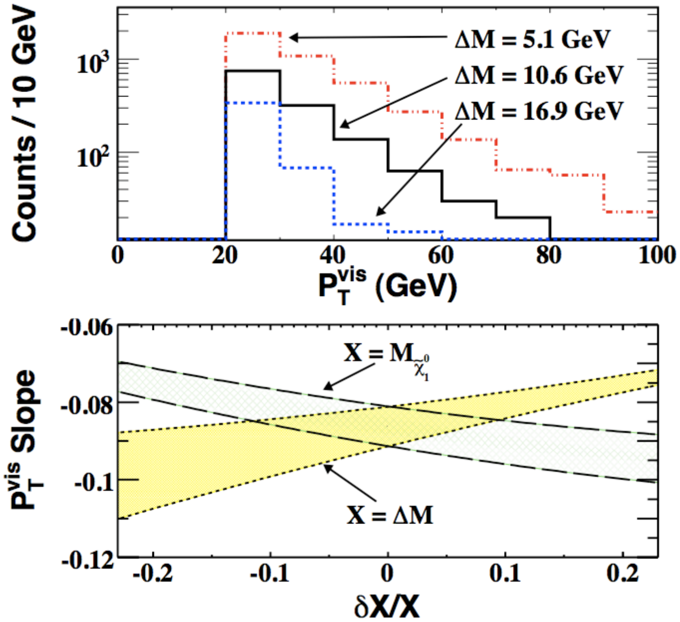

Figure 23: Co-annihilation p_T^{slope}. [Top] The visible transverse momentum, p_T, of low energy τ leptons. This plot shows the result of three different points in parameter space to show the dependence of the slope on ΔM. [Bottom] The functional behavior of p_T^{slope} as a function of the relative change of ΔM or $m_{\tilde{\chi}_1^0}$ from that of the co-annihilation benchmark point mass spectrum, shown in Table 3. The bands are the estimated 1σ contours for an integrated luminosity of 10 fb^-1 of data for the LHC running at 14 TeV center of mass collision energy.

pseudorapidity $|\eta| < 2.5$ and visible transverse momenta $p_T^{\mathrm{vis}} > 20$ GeV, except the leading tau which must have $p_T^{\mathrm{vis}} > 40$ GeV); (b) Number of jets in the event, $N_j \geq 2$ (for jets with pseudorapidity $|\eta| < 2.5$ and transverse momenta $p_T > 100$ GeV); (c) Missing transverse energy, $\not{E}_{\mathrm{T}} > 180$ GeV; (d) Scalar sum of leading jet transverse momenta and missing transverse energy, $\not{E}_{\mathrm{T}} + p_T^{\mathrm{jet}\ 1} + p_T^{\mathrm{jet}\ 2} > 600$ GeV; (e) No b-tagged jets with transverse momenta greater than either leading jet.

Once events have been selected in this way, we consider all tau lepton pairs in the event. We sort these tau pairs into OS and LS combinations in order to utilize the OS−LS subtraction technique described in Section 3.1. Then we use the information of these tau pairs to construct our observables.

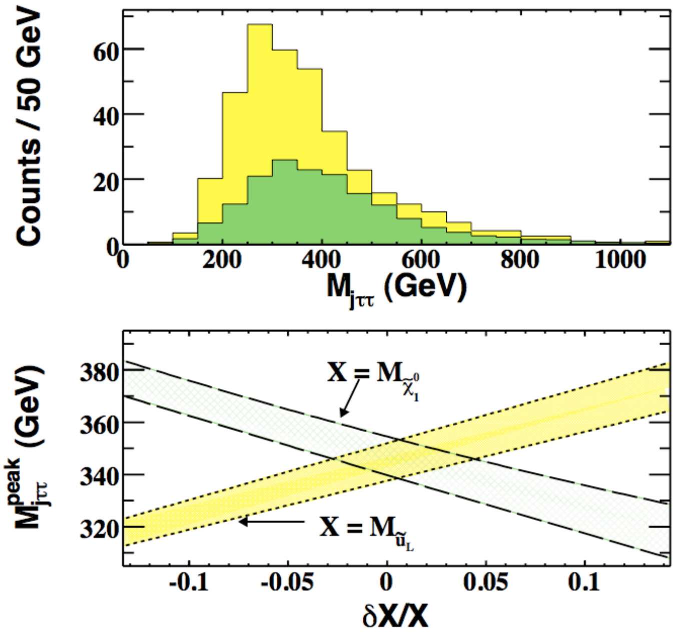

Figure 24: Co-annihilation $m_{J\tau\tau}$. [Top] The invariant mass, $m_{J\tau\tau}$. The yellow filled histogram is for a squark mass of $m_{\tilde{q}_L} = 660$ GeV, while the green filled histogram is for $m_{\tilde{q}_L} = 840$ GeV. All other SUSY masses are as listed in Table 3. [Bottom] The functional behavior of $m^{\text{peak}}_{J\tau\tau}$ as a function of the relative change of $m_{\tilde{q}_L}$ and $m_{\tilde{\chi}^0_1}$ from that of the co-annihilation benchmark point mass spectrum, shown in Table 3. The bands are the estimated 1σ contours for an integrated luminosity of 10 $\text{fb}^{-}1$ of data for the LHC running at 14 TeV center of mass collision energy.

The p_T^{slope} observable is simply formed by taking the lower p_T tau of each tau pair, and filling a histogram with it. By looking at the results for all of our model points, we see that the slope of this OS−LS histogram (plotted with a log-scale) is a very good function of ΔM. A plot showing the change in this slope for different ΔM values is shown in Figure 23. The functional behavior of p_T^{slope} with respect to ΔM and $m_{\tilde{\chi}^0_1}$ is shown in that figure as well.

The $m_{\tau\tau}$ observable is formed from the invariant mass of the tau pair. In this region, the resulting OS−LS histogram of $m_{\tau\tau}$ does not show a nice endpoint. However, the peak of the distribution, $m^{\text{peak}}_{\tau\tau}$, can be measured. This peak is a function of the SUSY masses $m_{\tilde{\tau}_1}$, $m_{\tilde{\chi}^0_2}$, and $m_{\tilde{\chi}^0_1}$. Alternatively, rather than measuring the stau mass by itself, we can measure instead ΔM.

The $m_{J\tau\tau}$ observable is formed from the invariant mass of the tau pair with the leading jets. We select all jets with $p_T > 100$ GeV to be leading jets in this case. For each tau pair, we compute $m_{J\tau\tau}$ for all such jets, and we order the results in order of decreasing $m_{J\tau\tau}$. We then select the second largest $m_{J\tau\tau}$ and use it to fill our $m_{J\tau\tau}^{\text{2nd}}$ histogram. For example, if a particular event has three jets with $p_T > 100$ GeV, then for every tau pair, we will have three values of $m_{J\tau\tau}$. We label them in order of decreasing $m_{J\tau\tau}$, such as $m_{J\tau\tau}^{\text{1st}} > m_{J\tau\tau}^{\text{2nd}} > m_{J\tau\tau}^{\text{3rd}}$. The $m_{J\tau\tau}^{\text{2nd}}$ distribution also fails to show a nice endpoint. So we once again measure the peak. This peak is a function of the SUSY masses $m_{\widetilde{q}_L}$, $m_{\widetilde{\chi}_2^0}$, and $m_{\widetilde{\chi}_1^0}$. The $m_{J\tau\tau}$ observable and its functional form are shown in Figure 24.

The $m_{J\tau}$ observable is formed similarly to the $m_{J\tau\tau}$ observable. However, since we only use one of the two tau leptons for every OS$-$LS pair, there are two possibilities for $m_{J\tau}$. In this region of parameter space, both of these possibilities form nice peaks which can be measured. Each of these peaks is a separate function of the SUSY masses $m_{\widetilde{q}_L}$, $m_{\widetilde{\chi}_2^0}$, $m_{\widetilde{\chi}_1^0}$, and ΔM. With this observable, we have now five measures of the Jet-τ-τ decay chain. Here, we can determine if ΔM is very small.

We still must determine the unification condition to see if we are in a mSUGRA model. Thus, we must also measure the gluino mass. This is because, due to the mass unification of the gauginos at the GUT scale of the theory, the neutralino and gluino masses must be in a certain ratio at the scale where we measure them. Namely, $m_{\widetilde{g}} : m_{\widetilde{\chi}_2^0} : m_{\widetilde{\chi}_1^0} \simeq 6 : 2 : 1$. Thus, if we also measure the gluino mass in some way, we can test this ratio.

The m_{eff} observable is always a function of the squark, gluino, and lightest neutralino masses, as discussed in Section 2. We can use this as another observable to find all five SUSY masses: $m_{\widetilde{g}}$, $m_{\widetilde{q}_L}$, $m_{\widetilde{\chi}_2^0}$, $m_{\widetilde{\chi}_1^0}$, and ΔM. Using these five SUSY masses, we can certainly verify that we are in the co-annihilation region of mSUGRA with both the small ΔM value, as well as the ratio of the gaugino masses. Thus, we must construct the m_{eff} observable.

To construct the m_{eff} observable, we use different selection cuts for our events. The

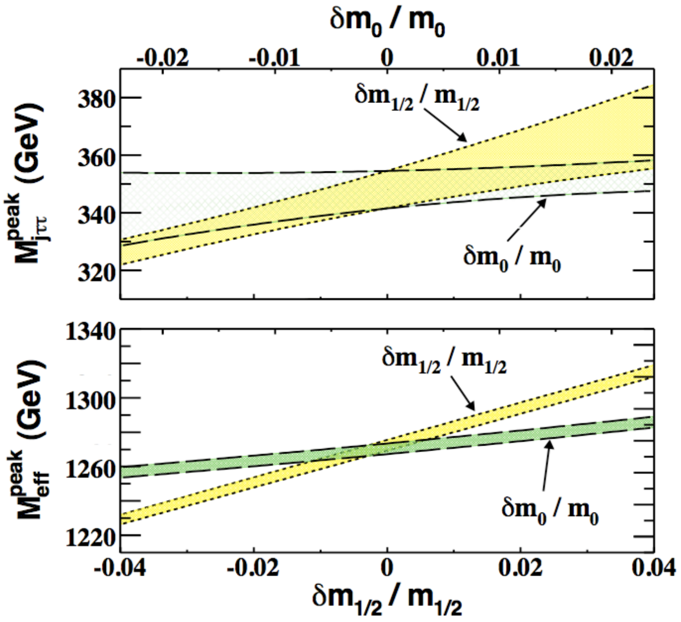

Figure 25: Co-annihilation $m_{J\tau\tau}$, m_{eff}. The functional behavior of [Top] $m^{\text{peak}}_{J\tau\tau}$ ([Bottom] $m^{\text{peak}}_{\text{eff}}$) as a function of the relative change of the model parameters m_0 or $m_{1/2}$ from that of the co-annihilation benchmark point, shown in Table 3. The bands are the estimated 1σ contours for an integrated luminosity of 10 fb$^{-}1$ of data for the LHC running at 14 TeV center of mass collision energy.

goal is to have an event with only jets, from gluino and squark decays, and missing energy from the lightest neutralino escaping the detector. Thus, we select events with the following cuts: (a) Number of jets $N_j \geq 4$ (for jets with pseudorapidity $|\eta| < 2.5$, transverse momenta $p_T > 50$ GeV, and not tagged as b-jets); (b) The leading jet $p_T > 400$ GeV; (c) Missing transverse energy $\not{E}_{\mathrm{T}} > 100$ GeV; (d) Transverse sphericity $S_T > 0.2$; (e) Number of isolated electrons or muons $N_{\updownarrow} = 0$ (for leptons with pseudorapidity $|\eta| < 2.5$ and transverse momenta $p_T > 15$ GeV). The peak of the m_{eff} distribution, combined with our other observables, gives us a measure of the gluino mass. Yet another observable we can use if we need it is m^b_{eff}. This observable is just the same as m_{eff}, except that the leading jet must be tagged as a b-jet. Once we check to see that the gaugino mass ratio is correct, we can assume a mSUGRA framework.

We then check the dependence of our physical observables as functions of the model

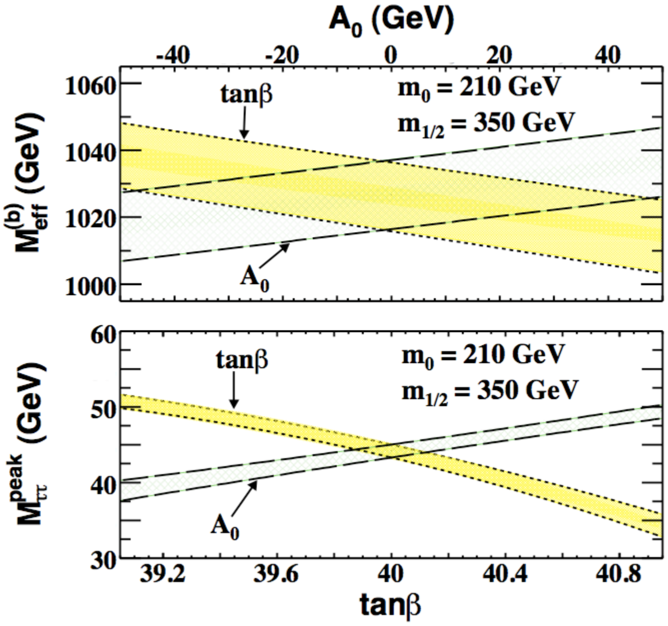

Figure 26: Co-annihilation $m_{\tau\tau}$, m^{b}_{eff}. The functional behavior of [Top] $m^{\text{peak}}_{\tau\tau}$ ([Bottom] $m^{b,\text{ peak}}_{\text{eff}}$) as a function of the change of the model parameters A_0 or $\tan\beta$ from that of the co-annihilation benchmark point, shown in Table 3. The bands are the estimated 1σ contours for an integrated luminosity of 10 fb$^-1$ of data for the LHC running at 14 TeV center of mass collision energy.

parameters, instead of just the individual masses. Here, we will need an additional observable which depends on the parameters A_0 and $\tan\beta$. To do this, we also investigate m^{b}_{eff}, which is sensitive to the third generation squarks. This observable is just the same as m_{eff}, with the exception that the leading jet be tagged as a b-jet. With this additional observable in hand, we choose at least four observables which are independent functions of the four model parameters, m_0, $m_{1/2}$, A_0, and $\tan\beta$. For instance, we can use the observables $m^{\text{peak}}_{\text{eff}}(m_0, m_{1/2})$, $m^{\text{peak}}_{J\tau\tau}(m_0, m_{1/2})$, $m^{b,\text{ peak}}_{\text{eff}}(m_0, m_{1/2}, A_0, \tan\beta)$, and $m^{\text{peak}}_{\tau\tau}(m_0, m_{1/2}, A_0, \tan\beta)$. Some of the functional forms of these observables can be seen plotted in Figures 24, 25, and 26. We can use the other observables as well to help reduce the uncertainty.

Once we have these functional forms, all we need to do to solve for the model parameters for any LHC measurements is to invert these functions. For instance, if

Table 4: Co-annihilation Measurement Results. Simulated measurements and uncertainties of the model parameters for the co-annihilation region benchmark point which is shown in Table 3. Also shown is the resulting calculated relative uncertainty for the dark matter relic density of the universe. All of the uncertainties estimated are for an integrated luminosity of 10 fb^{-1} of data for the LHC running at 14 TeV center of mass collision energy.

m_0	$m_{1/2}$	A_0	$\tan\beta$	$\delta\Omega_{\widetilde{\chi}_1^0}/\Omega_{\widetilde{\chi}_1^0}$
205 ± 4 GeV	350 ± 4 GeV	0 ± 16 GeV	40 ± 1	11%

our benchmark point is measured at the LHC, we will get the measurements and uncertainties $m_{\text{eff}}^{\text{peak}}$, $m_{J\tau\tau}^{\text{peak}}$, $m_{\text{eff}}^{b,\text{ peak}}$, and $m_{\tau\tau}^{\text{peak}}$. They will each have their own uncertainties. Using these values in the functional forms gives us four equations for the four unknown model parameters. All we must do is solve these four equations for the model parameters m_0, $m_{1/2}$, A_0, and $\tan\beta$. We can solve them either analytically or numerically. To find the uncertainties in each of these measurements, we can write a simple Monte Carlo program. This program repeats the above process many times, each time choosing a random value for the measurements based upon their uncertainty. The result of this will be a solution for each model parameter which is a distribution of values. We can find the uncertainty of these model parameters by fitting each distribution with a Gaussian function. The result of this kind of analysis is shown in Table 4, which shows the estimated uncertainties for all the model parameters.

Once we have these model parameters in hand, we can use them to infer the remainder of the SUSY particle masses. With the full mass spectrum in hand, we can return to our original motivation for this study: Investigating the properties of the dark matter particle. The full mass spectrum allows us to calculate the dark matter relic density of the universe. We can compare the result this calculation, made only with the results of LHC data and the cosmological calculation, to that of WMAP's measured value for the dark matter relic density. The result for this simulated study is that the dark matter relic density agrees well with the WMAP experiment, and has a rather small uncertainty. The uncertainty is reported in

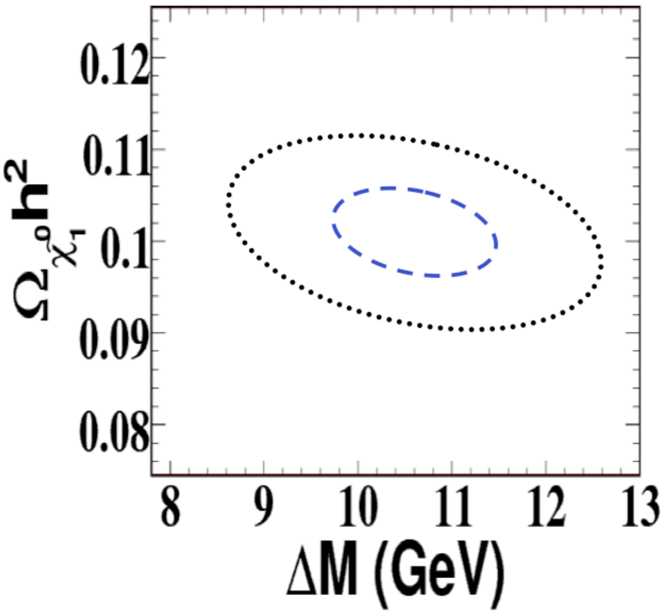

Figure 27: Co-annihilation Error Ellipse. The 1σ uncertainty contour in the ΔM-$\Omega_{\tilde{\chi}_1^0}h^2$ plane. The dotted black line is for an integrated luminosity of 10 fb^{-1}, whereas the blue dashed line is for 50 fb^{-1}.

Table 4. Since the dark matter relic density is most sensitive to the value of ΔM in this region, we plot the 1σ error ellipse in the ΔM-$\Omega_{\tilde{\chi}_1^0}h^2$ plane. This plot is shown in Figure 27.

4.2 Overabundance Region

The overabundance region of mSUGRA is usually ignored, due to the fact that under the standard cosmological calculation, there is too much dark matter to agree with the WMAP experiment in this region. However, the relic density calculation itself can be influenced by different models. For instance, the Supercritical String Cosmology (SSC) [24] alters the way the relic density is calculated. The basic idea of the SSC is to explain the Dark Energy content of the universe. The dark energy has two components in this framework. One component arises from a time dependent dilaton field, and the other from the Q^2 associated

Table 5: SSC Higgs Point SUSY Mass Spectrum. SUSY particle masses (in GeV) for the SSC region benchmark point: $m_0 = 471$ GeV, $m_{1/2} = 440$ GeV, $\tan\beta = 40$, $A_0 = 0$, and $\mu > 0$. Also shown are the dominant branching ratios of the $\widetilde{\chi}_2^0$ decay.

$\widetilde{g}$	$\widetilde{u}_L$ $\widetilde{u}_R$	$\widetilde{t}_2$ $\widetilde{t}_1$	$\widetilde{b}_2$ $\widetilde{b}_1$	$\widetilde{e}_L$ $\widetilde{e}_R$	$\widetilde{\tau}_2$ $\widetilde{\tau}_1$	$\widetilde{\chi}_2^0$ $\widetilde{\chi}_1^0$	$\mathcal{B}(\widetilde{\chi}_2^0 \to h^0\widetilde{\chi}_1^0)(\%)$ $\mathcal{B}(\widetilde{\chi}_2^0 \to Z^0\widetilde{\chi}_1^0)(\%)$
1041	1044 1017	954 768	958 899	557 500	532 393	341 181	86.8 13.0

with the central charge deficit.

The time dependent dilaton field, ϕ, also has another effect on our reality besides just helping to explain dark energy. Due to its time dependence, the Liouville operator gets altered. This operator is involved in the proper time derivatives in the cosmology. Thus, the usual Boltzman equation, shown in Equation (1.1), gets modified:

$$\frac{\mathrm{d}n}{\mathrm{d}t} + 3Hn + \langle\sigma v\rangle \left(n^2 - n_{eq}^2\right) - \dot{\phi}n = 0 \tag{4.1}$$

Under the modified calculation, the relic density is a factor of ten smaller than it would be for the standard calculation. Thus, the overabundance region becomes an allowed region under the influence of the SSC. The region in parameter space where dark matter is allowed is much wider than the co-annihilation region. This can be seen visually in Figure 28.

Due to the size of the region allowed by WMAP under the SSC, there are various signals to study at the LHC [25]. Very often in SUSY events in this region of parameter space, there are a large amount of $\widetilde{\chi}_2^0$ particles produced. Figure 29 shows the dominant decay branching ratios for these particles with different choices of allowed parameter values. These branching ratios tell us what signals we can expect to see at the LHC for different sets of model parameters.

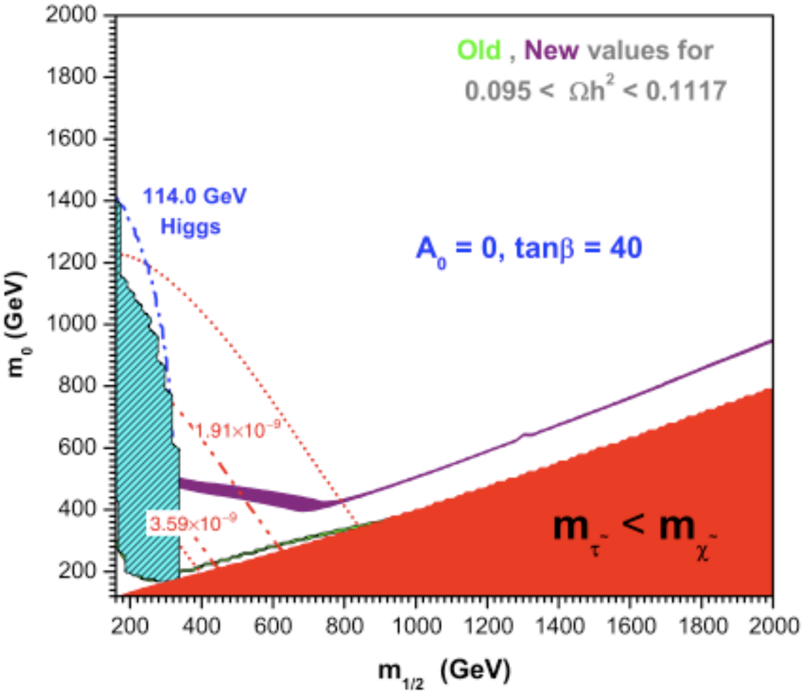

Figure 28: WMAP Allowed Region. The parameter space as allowed by the WMAP constraint on the dark matter relic density. This plot shows parameter space for $A_0 = 0$ and $\tan\beta = 40$. The very thin green band is the allowed region under the standard cosmology. The dark purple band is the allowed region under the SSC calculation. Also shown in the plot are excluded regions. The red region does not have the lightest neutralino as the stable lightest SUSY particle. The hatched cyan region is excluded by experimental bounds on the rare decay $b \to s\gamma$. The Higgs mass lower boundary is shown as a dashed-dotted blue line. Muon $g_\mu - 2$ boundaries are shown as dashed and dotted red lines.

Here, we examine three benchmark points within the SSC allowed region. The partial SUSY mass spectrum and dominant branching ratios of observable decay chains for these three points are shown in Tables 5, 6, and 7. We examine these benchmark points in the same manner as we examined the co-annihilation benchmark point. We plan our observables by looking at the dominant decay chains of the event. We then choose observables which partially reconstruct those decay chains. By considering the SM backgrounds for these observables, we select events with some cuts to help remove such backgrounds. To see how the observables act as functions of the model parameters, we generate data for points

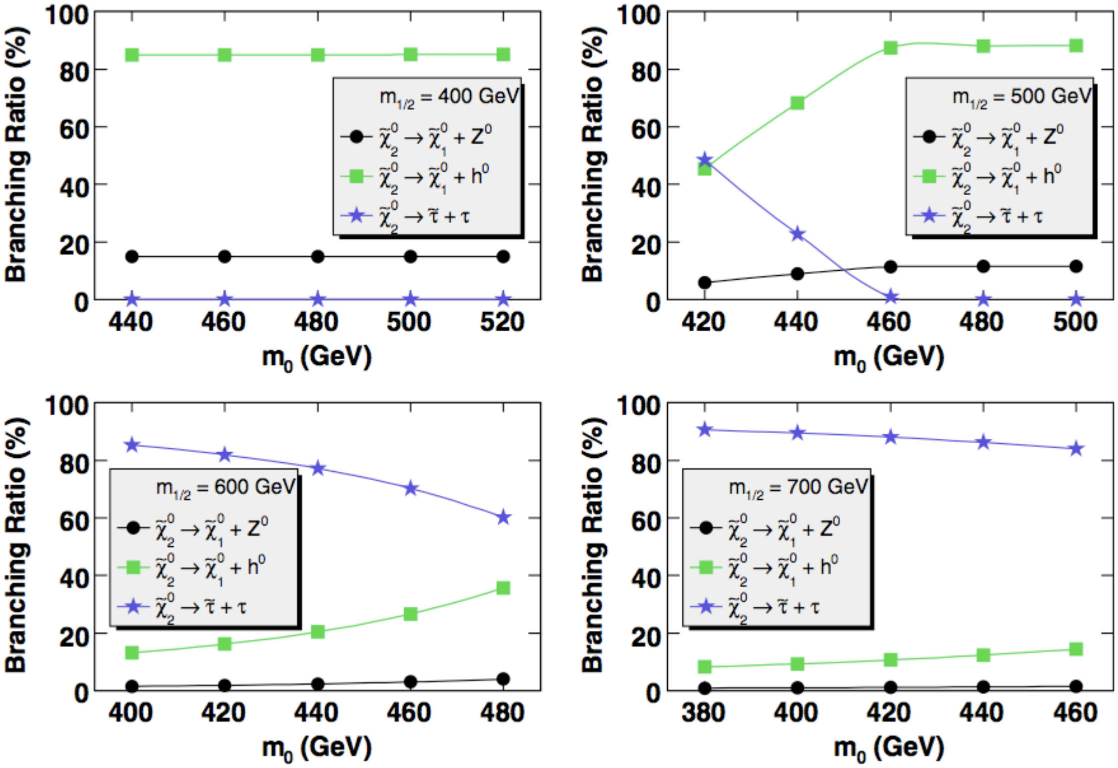

Figure 29: SSC Branching Ratios. Dominant branching ratios for decays of the $\widetilde{\chi}_2^0$ for different parameter values in the SSC allowed region of parameter space (as seen in Figure 28). These plots all have the parameter values $A_0 = 0$ and $\tan\beta = 40$.

which vary one parameter at a time while holding the others constant. Using these data sets, we find the functional forms of the observables as a function of the model parameters. Finally, we can use the model parameters to infer the rest of the model and calculate the dark matter relic density of the universe.

For the benchmark point shown in Table 5, the dominant decay chain we analyze is the Higgs-plus-Jet decay chain, $\widetilde{q}_L \rightarrow q\widetilde{\chi}_2^0 \rightarrow qh^0\widetilde{\chi}_1^0$, which is shown in Figure 10. To partially reconstruct this decay chain, we use the endpoint $m_{Jh^0}^{\max}$. This endpoint is theoretically predicted to be that of Equation (2.13) with the assignments $A \equiv m_{\widetilde{q}_L}^2/m_{\widetilde{\chi}_2^0}^2$, $B \equiv m_{\widetilde{\chi}_1^0}^2/m_{\widetilde{\chi}_2^0}^2$, and $C \equiv m_h^2/m_{\widetilde{\chi}_2^0}^2$. In order to reconstruct this endpoint, we must first reconstruct the Higgs boson, h^0, which decays primarily to b-jets. To select events to construct this observable, we use the following selection

Table 6: SSC Z Point SUSY Mass Spectrum. SUSY particle masses (in GeV) for the SSC region benchmark point: $m_0 = 471$ GeV, $m_{1/2} = 320$ GeV, $\tan\beta = 40$, $A_0 = 0$, and $\mu > 0$. Also shown are the dominant branching ratios of the $\widetilde{\chi}_2^0$ decay. This benchmark point is excluded by the bound on the $b \to s\gamma$ decay branching ratio. However, we examine it here to demonstrate the technique used to reconstruct mSUGRA models.

$\widetilde{g}$	$\widetilde{u}_L$ $\widetilde{u}_R$	$\widetilde{t}_2$ $\widetilde{t}_1$	$\widetilde{b}_2$ $\widetilde{b}_1$	$\widetilde{e}_L$ $\widetilde{e}_R$	$\widetilde{\tau}_2$ $\widetilde{\tau}_1$	$\widetilde{\chi}_2^0$ $\widetilde{\chi}_1^0$	$\mathcal{B}(\widetilde{\chi}_2^0 \to h^0\widetilde{\chi}_1^0)(\%)$ $\mathcal{B}(\widetilde{\chi}_2^0 \to Z^0\widetilde{\chi}_1^0)(\%)$
785	838 821	763 598	768 708	519 487	493 389	241 129	0.0 99.6

Table 7: SSC τ Point SUSY Mass Spectrum. SUSY particle masses (in GeV) for the SSC region benchmark point: $m_0 = 440$ GeV, $m_{1/2} = 600$ GeV, $\tan\beta = 40$, $A_0 = 0$, and $\mu > 0$. Also shown are the dominant branching ratios of the $\widetilde{\chi}_2^0$ decay.

$\widetilde{g}$	$\widetilde{u}_L$ $\widetilde{u}_R$	$\widetilde{t}_2$ $\widetilde{t}_1$	$\widetilde{b}_2$ $\widetilde{b}_1$	$\widetilde{e}_L$ $\widetilde{e}_R$	$\widetilde{\tau}_2$ $\widetilde{\tau}_1$	$\widetilde{\chi}_2^0$ $\widetilde{\chi}_1^0$	$\mathcal{B}(\widetilde{\chi}_2^0 \to h^0\widetilde{\chi}_1^0)(\%)$ $\mathcal{B}(\widetilde{\chi}_2^0 \to \tau\widetilde{\tau}_1)(\%)$
1366	1252 1211	1153 957	1153 1094	594 494	574 376	462 249	20.5 77.0

cuts: (a) Number of b tagged jets in the event, $N_b \geq 2$ (for b-jets with pseudorapidity $|\eta| \leq 1.5$ and visible transverse momenta $p_T^{\text{vis}} \geq 100$ GeV); (b) Number of jets in the event, $N_j \geq 4$ (for jets which are not b tagged with pseudorapidity $|\eta| < 2.5$ and transverse momenta $p_T > 200$ GeV); (c) Missing transverse energy, $\not{E}_{\text{T}} > 180$ GeV; (d) Scalar sum of leading jet transverse momenta and missing transverse energy, $\not{E}_{\text{T}} + p_T^{\text{jet }1} + p_T^{\text{jet }2} > 600$ GeV. These cuts remove the majority of SM background events from sources such as $t\bar{t}$, $W+$Jets, and $Z+$Jets. These cuts also remove some of the background from SUSY events which do not contain the Higgs-plus-Jet decay chain.

To reconstruct the Higgs boson in this decay chain, we select b-jet pairs from the events which survive the above cuts. These b tagged jets must each have $p_T \geq 100$ GeV. Each b pair must have $0.4 < \Delta R_{bb} < 1$. For this cut, the lower ΔR limit is due to the jet separation requirements of the detection of jets. The upper limit is selected because the b quarks get a boost from the Higgs momentum, causing them to be closer together. Random b-jet pairs do not receive such a boost. Thus, $\Delta R_{bb} < 1$ is a good cut to help remove some combinatoric background of b-jet pairs while reconstructing the Higgs.

When we form the b-jet pair invariant mass, we see a Higgs boson mass peak between 100 and 120 GeV, as well as a background distribution around it. This is the perfect situation for a sideband subtraction, as discussed in Section 3.3. We use $100\text{ GeV} \leq m_{bb} \leq 120\text{ GeV}$ for the Higgs mass window, and $70\text{ GeV} \leq m_{bb} \leq 90\text{ GeV}$ and $130\text{ GeV} \leq m_{bb} \leq 150\text{ GeV}$ for the sideband windows. Using these b-jet pairs, we combine with the leading jets to form the invariant mass, m_{Jbb}. Since there are two leading jets per event, we sort the combinations by the value of the invariant mass, i.e. $m_{Jbb}^{\text{1st}} > m_{Jbb}^{\text{2nd}}$. We select the second highest invariant mass, m_{Jbb}^{2nd}, for each b-jet pair, and we perform the sideband subtraction, resulting in the $m_{Jbb}^{\text{2nd, SS}}$ distribution. This distribution has a nice endpoint which can be found by a fit. This process could be improved if we used the BEST to remove some of the combinatoric background of leading jets. This technique is described in Section 3.2.

For the next benchmark point, shown in Table 6, the decay chain we wish to reconstruct is similar to that of the Higgs-plus-Jet decay chain. The only difference is a Z boson in the chain rather than a Higgs boson: $\widetilde{q}_L \to q\widetilde{\chi}_2^0 \to qZ^0\widetilde{\chi}_1^0$. This Z-plus-Jet decay chain is much easier to reconstruct than the Higgs-plus-Jet decay chain, since the Z boson has the convenient decay channel into lepton pairs. Thus, we can reconstruct the Z boson simply from oppositely charged electrons or oppositely charged muons. Then we combine the reconstructed Z boson with the leading jets as we did for the Higgs-plus-Jet decay chain. We select events with the same selection cuts as for the Higgs-plus-Jet decay chain.

To help in the Z boson reconstruction, we use a technique similar to the OS$-$LS technique described in Section 3.1. Here, instead of sorting electrons and muons by opposite-sign and like-sign (OS and LS) pairs, we sort them instead by opposite-sign-same-flavor and opposite-sign-opposite-flavor pairs (OSSF and

OSOF). The OSSF pairs are $e^{\pm}e^{\mp}$ and $\mu^{\pm}\mu^{\mp}$, whereas the OSOF pairs are $e^{\pm}\mu^{\mp}$ and $\mu^{\pm}e^{\mp}$. The reason for selecting these leptons in this manner is just the same reason for the OS−LS subtraction: The Z bosons conserve flavor as they decay, so the OSSF di-lepton distribution, $m_{e^{\pm}e^{\mp},\mu^{\pm}\mu^{\mp}}$, will contain some of the Z boson signal we want, as well as some combinatoric background. However, the OSOF di-lepton distribution, $m_{e^{\pm}\mu^{\mp},\mu^{\pm}e^{\mp}}$, contains only combinatoric background, and models that background well. Thus, the OSSF−OSOF subtraction behaves for this case just like the OS−LS subtraction does for the tau decay chains discussed in Section 3.1.

With the Z boson reconstructed by these leptons and selected by its mass, we combine it with the leading jets to form the invariant mass $m_{J\ell\ell}$, just as we did for the Higgs boson . Once again, we sort these by the invariant mass, $m_{J\ell\ell}^{\text{1st}} > m_{J\ell\ell}^{\text{2nd}}$. We select the second one, performing the OSSF−OSOF subtraction as well as selecting the lepton pairs by the Z boson mass, giving us the Z-plus-Jet reconstruction observable $m_{J\ell\ell}^{\text{2nd, OSSF}-\text{OSOF}}$. This distribution shows a nice endpoint, which we can again find by performing a simple fit. Once again, this process could be improved if we use the BEST.

The final benchmark point we study in this overabundance region is very much like the co-annihilation signal. The decay chain we reconstruct is the Jet-τ-τ decay chain, and the analysis of it is very similar. The difference between this benchmark point and the co-annihilation region is that there is not a small mass difference between the lightest stau and lightest neutralino. The event selection cuts for this point are just the same as for the co-annihilation region, with the exception that the leading tau must only have $p_T^{\text{vis}} > 20$ GeV. The observables we construct are just the same as what has been described in Section 4.1.

In all of these regions, we need at least four observables to fully reconstruct the model. The effective mass distributions, m_{eff}, m_{eff}^{b}, and m_{eff}^{2b}, can be used as the additional observables in any region of parameter space. The effective mass distributions m_{eff} and m_{eff}^{b} were used in the co-annihilation region described in Section 4.1. These observables are used in an identical way for these overabundace

Table 8: SSC Measurement Results. Simulated measurements and uncertainties of the model parameters for the Higgs-plus-Jet and Jet-τ-τ overabundance benchmark points shown in Tables 5 and 7. The result for the Z-plus-Jet benchmark point from Table 6 is not shown here, since that benchmark point is excluded by the bound on the branching ratio of the $b \to s\gamma$ decay. Also shown is the resulting calculated relative uncertainty for the dark matter relic density of the universe. The required integrated luminosity of data for the LHC running at 14 TeV center of mass collision energy is also shown.

Signal $\mathcal{L}$	Higgs-plus-Jet 1000 fb^{-1}	Jet-τ-τ 500 fb^{-1}
m_0	472 ± 50 GeV	440 ± 23 GeV
$m_{1/2}$	440 ± 15 GeV	600 ± 6 GeV
A_0	0 ± 95 GeV	0 ± 45 GeV
$\tan\beta$	39 ± 17	40.0 ± 2.7
$\delta\Omega_{\widetilde{\chi}_1^0}/\Omega_{\widetilde{\chi}_1^0}$	150%	18.4%

benchmark points. The effective mass distribution, m_{eff}^{2b}, is just the same as the m_{eff}^{b}, with the exception that both leading jets must be b tagged jets.

Using all of our observables together for each benchmark point, we can see how well the LHC performs at reconstructing the mSUGRA model in each of these regions of parameter space. The observables for the Higgs-plus-Jet benchmark point have the functional forms as follows: $m_{\text{eff}}^{\text{peak}} = f_1(m_0, m_{1/2})$, $m_{\text{eff}}^{b,\text{ peak}} = f_2(m_0, m_{1/2}, A_0, \tan\beta)$, $m_{\text{eff}}^{2b,\text{ peak}} = f_3(m_0, m_{1/2}, A_0, \tan\beta)$, and the Higgs-plus-Jet invariant mass, $m_{Jbb}^{\text{2nd, max}} = f_4(m_0, m_{1/2})$. For the Z-plus-Jet benchmark point, the observables are the same, except we use the Z-plus-Jet endpoint instead of the Higgs-plus-Jet endpoint. Lastly, for the Jet-τ-τ benchmark point, we use the observables: $m_{\text{eff}}^{\text{peak}} = f_1(m_0, m_{1/2})$, $m_{\text{eff}}^{b,\text{ peak}} = f_2(m_0, m_{1/2}, A_0, \tan\beta)$, the ditau invariant mass $m_{\tau\tau}^{\text{OS}-\text{LS, peak}} = f_3(m_0, m_{1/2}, A_0, \tan\beta)$, and the Jet-$\tau$-$\tau$ invariant mass $m_{J\tau\tau}^{\text{OS}-\text{LS, 2nd, peak}} = f_4(m_0, m_{1/2})$.

We can then invert the functional forms for each region numerically, and use simple Monte Carlo programs to estimate the uncertainty in the result. The resulting parameters and their uncertainties we find with this process are shown in Table 8.

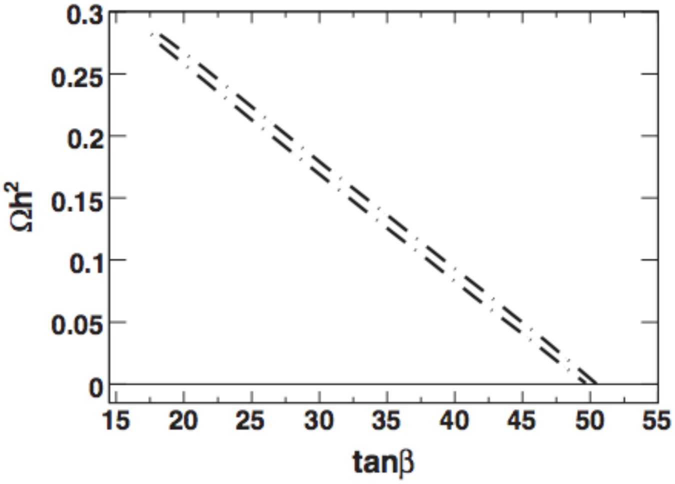

Figure 30: SSC Error Ellipse. The 1σ uncertainty contour in the $\tan\beta$-$\Omega_{\tilde{\chi}_1^0}h^2$ plane. This result was obtained for the Higgs-plus-Jet overabundance benchmark point for an integrated luminosity of 1000 fb^{-1}.

Table 8 also shows the resulting uncertainty in the dark matter relic density which is found using DARKSUSY. For the Higgs-plus-Jet overabundance benchmark point, the uncertainty in the dark matter relic density is dominated by the uncertainty in the determination of $\tan\beta$. Thus, we show the 1σ error ellipse in the $\tan\beta$-$\Omega_{\tilde{\chi}_1^0}h^2$ plane in Figure 30. The results for this region of parameter space are not as good as the results for the co-annihilation region. However, a lot of this is simply due to the fact that, in this overabundance region, the SUSY particle masses are much heavier. Also, the Higgs-plus-Jet and Z-plus-Jet decay chains are very difficult, either due to using b-jets to reconstruct a Higgs boson, or due to the small $Z \to \ell\ell$ branching ratio.

4.3 Focus Point or Hyperbolic Branch Region

The *Focus Point* or *Hyperbolic Branch* region [26] of mSUGRA is a region of parameter space with a very large value for m_0. Typically in this region, $m_0 \simeq 2$ TeV. Having such a large value of m_0 has an effect on the electroweak symmetry breaking condition. Due to this, the value of the bilinear Higgs

Table 9: Focus Point SUSY Mass Spectrum. SUSY particle masses (in GeV) for the Focus Point region benchmark point: $m_0 = 3550$ GeV, $m_{1/2} = 314$ GeV, $\tan\beta = 10$, $A_0 = 0$.

$\widetilde{g}$	$\widetilde{u}_L$ $\widetilde{u}_R$	$\widetilde{t}_2$ $\widetilde{t}_1$	$\widetilde{b}_2$ $\widetilde{b}_1$	$\widetilde{e}_L$ $\widetilde{e}_R$	$\widetilde{\tau}_2$ $\widetilde{\tau}_1$	$\widetilde{\chi}^0_4$ $\widetilde{\chi}^0_3$ $\widetilde{\chi}^0_2$ $\widetilde{\chi}^0_1$	$\widetilde{\chi}^\pm_2$ $\widetilde{\chi}^\pm_1$
889	3572 3582	2089 2938	2927 3553	3549 3548	3519 3534	307 197 175 116	299 165

parameter μ gets *focused* to a much smaller value than in other regions of mSUGRA. This small μ parameter means that the dark matter particle, the lightest neutralino, becomes Higgsino-like. This Higgsino-like neutralino hass similar interactions as a Higgs boson, which means that it will couple strongly to massive particles whenever such interactions are allowed. This allows for the annihilation of dark matter via heavy boson mediators, such as the Higgs or Z boson. This is the mechanism which allows for the correct amount of dark matter in the universe in this region.

The large value of m_0 has another effect, which is like a double-edged sword. The sleptons and squarks in this region of parameter space are so massive that they are effectively decoupled from the theory at the LHC energy scale. The problem with this is that we can never measure m_0 in this model at the LHC. However, there is a benefit as well: The dark matter calculation is independent of m_0 in this region. Even though the Higgsino-like dark matter particle couples strongly to massive particles, two such dark matter particles cannot couple to a slepton or squark due to the R-parity conservation. Thus, in this region, the dark matter content of the universe is mostly dependent on the values of $m_{1/2}$, μ, and $\tan\beta$ [27].

If we see a Focus Point like signature at the LHC, we can treat the model as if it only had three parameters. To show this, we select a benchmark point within the

Focus Point region. The model parameters for our benchmark point are $m_0 = 3550$ GeV, $m_{1/2} = 314$ GeV, $A_0 = 0$, $\tan\beta = 10$, and sign$\mu > 0$. The mass spectrum for such a benchmark point is shown in Table 9. There are many signals in this region from many different decay chains. However, in this regioin of parameter space, certain decays are much easier to reconstruct than others. For instance, $\widetilde{\chi}_2^0$ and $\widetilde{\chi}_3^0$ can both undergo a three body decay to $\widetilde{\chi}_1^0$ and e^+e^- or $\mu^+\mu^-$, both with a branching ratio around 6.5%. Although the branching ratio is not very large, reconstructing decays with leptons is very easy experimentally. Also, because the decay of the $\widetilde{\chi}_2^0$ and $\widetilde{\chi}_3^0$ have the same decay products and similar branching ratios, the same distribution may show two endpoints. Each endpoint will be proportional to the mass difference of the decay in question. i.e. $\Delta_{21} \equiv m_{\widetilde{\chi}_2^0} - m_{\widetilde{\chi}_1^0}$ and $\Delta_{31} \equiv m_{\widetilde{\chi}_3^0} - m_{\widetilde{\chi}_1^0}$.

If we can determine Δ_{21} and Δ_{31} from this endpoint measurement, as well as the gluino mass, $m_{\widetilde{g}}$, we can reconstruct the whole (three parameter) model in this region. This is because $m_{\widetilde{g}}$ basically determines $m_{1/2}$, while the neutralino measurements Δ_{21} and Δ_{31} determine μ and $\tan\beta$ once $m_{1/2}$ is known. We can estimate based upon potential measurements of $m_{\widetilde{g}}$, Δ_{21}, and Δ_{31} what the measurement accuracy are for $m_{1/2}$, μ, and $\tan\beta$, as well as for the dark matter relic density, Ωh^2. The result of such a study shows that for input measurement uncertainties of $\delta\Delta_{21}/\Delta_{21} = 1.7\%$, $\delta\Delta_{31}/\Delta_{31} = 1.2\%$, and $\delta m_{\widetilde{g}}/m_{\widetilde{g}} = 4.5\%$, the estimated upper bound uncertainties for the model parameters and relic density are $\delta m_{1/2}/m_{1/2} = 4.5\%$, $\delta\mu/\mu = 4.5\%$, and $\delta\Omega h^2/\Omega h^2 = 42\%$.

4.4 Non-Universal Supergravity

We have examined these mSUGRA scenarios thoroughly. However, nature may not be so kind as to give us a simple four parameter model. Thus, we must also be ready to find SUSY particles in models more general than the mSUGRA model. One way to do this is to take a small generalization of the mSUGRA model and see if we can still fully reconstruct the model. A natural generalization of mSUGRA is to relax the constraint of the unification of SUSY particle masses at the GUT

Table 10: nuSUGRA SUSY Mass Spectrum. SUSY particle masses (in GeV) for the nuSUGRA benchmark point: $m_0 = 360$ GeV, $m_{1/2} = 500$ GeV, $\tan\beta = 40$, $A_0 = 0$, and $m_H = 732$ GeV. Also shown is the value for the Higgs bilinear coupling, μ.

$\widetilde{g}$	$\widetilde{u}_L$ $\widetilde{u}_R$	$\widetilde{t}_2$ $\widetilde{t}_1$	$\widetilde{b}_2$ $\widetilde{b}_1$	$\widetilde{e}_L$ $\widetilde{e}_R$	$\widetilde{\tau}_2$ $\widetilde{\tau}_1$	$\widetilde{\chi}_4^0$ $\widetilde{\chi}_3^0$ $\widetilde{\chi}_2^0$ $\widetilde{\chi}_1^0$	$\widetilde{\chi}_2^\pm$ $\widetilde{\chi}_1^\pm$	μ
1161	1113 1078	992 781	989 946	494 407	446 225	432 316 293 199	427 291	307

scale [28]. This is called Non-Universal Supergravity (nuSUGRA).

For our nuSUGRA study [29], we relax the scalar particle unification at the GUT scale. Specifically, we allow the Higgs boson masses to have a different value at the GUT scale than all the scalar superpartners of the SM fermions. This Higgs mass non-universality can drastically change the SUSY particle mass spectrum from the mSUGRA model. Since the Higgs mass is closely linked to the electroweak symmetry breaking condition and the bilinear Higgs parameter μ, the Higgs mass non-universality effectively promotes μ to a free parameter. Changing the value of μ affects the neutralino masses, which means that the ratio of gluino mass to neutralino masses, $m_{\widetilde{g}} : m_{\widetilde{\chi}_2^0} : m_{\widetilde{\chi}_1^0}$, becomes very different for nuSUGRA than mSUGRA. When we measure this ratio, we can easily discriminate between the nuSUGRA and mSUGRA models.

We start our study of this model as we did for the other mSUGRA regions by selecting a benchmark point which predicts the correct dark matter content of the universe today. We choose a point which has the same mechanism for the correct dark matter content as the Focus Point region. To achieve this, we start in the overabundance region of mSUGRA, then increase the value of the Higgs boson masses at the GUT scale. This reduces the value of the parameter μ to be quite small. This means that we have a Higgsino-like dark matter particle just like in the

Table 11: nuSUGRA Measurement Results. Simulated measurements and uncertainties of the model parameters for the nuSUGRA model benchmark point which is shown in Table 10. Also shown is the value for the bilinear Higgs parameter, μ, and the resulting calculated relative uncertainty for the dark matter relic density of the universe. All of the uncertainties estimated are for the LHC running at 14 TeV center of mass collision energy.

$\mathcal{L}$ (fb^{-1})	1000 fb^{-1}	100 fb^{-1}	(Systematic)
$m_{1/2}$ (GeV)	500 ± 3	500 ± 9	± 10
m_H (GeV)	727 ± 10	727 ± 13	± 15
m_0 (GeV)	366 ± 26	367 ± 57	± 56
A_0 (GeV)	3 ± 34	0 ± 73	± 66
$\tan\beta$	39.5 ± 3.8	39.5 ± 4.6	± 4.5
μ (GeV)	321 ± 25	331 ± 48	± 48
$\Omega_{\widetilde{\chi}_1^0}$	$0.094^{+0.107}_{-0.038}$	$0.088^{+0.168}_{-0.072}$	$^{+0.175}_{-0.072}$

Focus Point region. The model parameters and SUSY mass spectrum for our benchmark point is shown in Table 10.

There are two predominant decay chains to examine within this nuSUGRA region. The first is a Jet-τ-τ decay chain like that of the co-annihilation region. We can analyze this in just the same manner as we did in Section 4.1. The other signal comes from the W-plus-Jet decay chain: $\widetilde{q} \to q\widetilde{\chi}_1^{\pm}\,(\widetilde{\chi}_4^0) \to qW^{\pm}\widetilde{\chi}_1^0\,\left(\widetilde{\chi}_1^{\mp}\right)$. This decay chain is illustrated in Figure 5. We can analyze this decay chain just as we did in Section 3.4.

To once again demonstrate the power of BEST, we use it to analyze this decay chain even in the presence of full SM background. To simulate events for this demonstration, we once again use PYTHIA and PGS4. The SUSY mass spectrum is generated using ISAJET [10]. We also use ALPGEN to simulate some SM backgrounds. The primary SM backgrounds for the events we wish to analyze are Z+jets, W+jets, and $t\bar{t}$ events. We mix these SM backgrounds in randomly with our SUSY signal events according to cross-section.

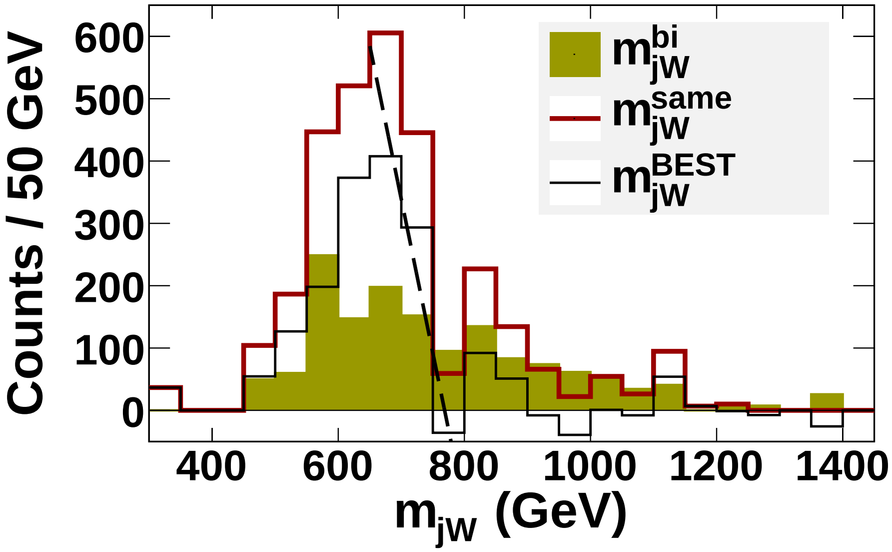

Figure 31: nuSUGRA m_{JW}. The W plus jet invariant mass distribution, m_{jW}. This plot was This plot shows the same-event, bi-event, and BEST distributions as described in the text. BEST removes the background obscuring the endpoint. For an integrated luminosity of 100 fb^{-1}, we find the endpoint to be 769 ± 18 GeV. This is within 2σ of the theoretical endpoint, which is 738.8 GeV for the most probable decay chain of this type, $\tilde{q} \to q + \tilde{\chi}_4^0 \to q + W^{\pm} + \tilde{\chi}_1^{\mp}$.

To help reduce the SM backgrounds, we use the following selection cuts, which are refined from the cuts in [29]: (i) Missing transverse energy, $\not{E}_{\rm T} \geq 180$ GeV; (ii) Number of jets, $N_j \geq 4$, where $p_T^{(j)} \geq 30$ GeV; (iii) Minimum $\Delta\phi$ between leading three jets and missing transverse energy, $\Delta\phi_{\rm min} \geq 0.5$; (iv) Leading jet transverse momenta, $p_T^{(1\text{st } j)} \geq 300$ GeV and $p_T^{(2\text{nd } j)} \geq 200$ GeV; (v) ΔR between leading jets, $\Delta R(1\text{st } j, 2\text{nd } j) \leq 3.2$; (vi) Scalar sum, $p_T^{(1\text{st } j)} + p_T^{(2\text{nd } j)} + 3 \cdot \not{E}_{\rm T} \geq 1600$ GeV. Once these selection cuts are performed, we construct the W plus jet invariant mass distribution just as described in Section 3.4. The result of this process is shown in Figure 31.

In addition to the four observables described above, we can also use the effective mass observable, $m_{\rm eff}$, as a fifth observable with which to fully reconstruct the model. Thus, the observables of this nuSUGRA benchmark point have the functional forms as follows: $m_{\rm eff}^{\rm peak} = f_1(m_{1/2})$, $m_{Jjj}^{\rm max} = f_2(m_{1/2}, m_H)$,

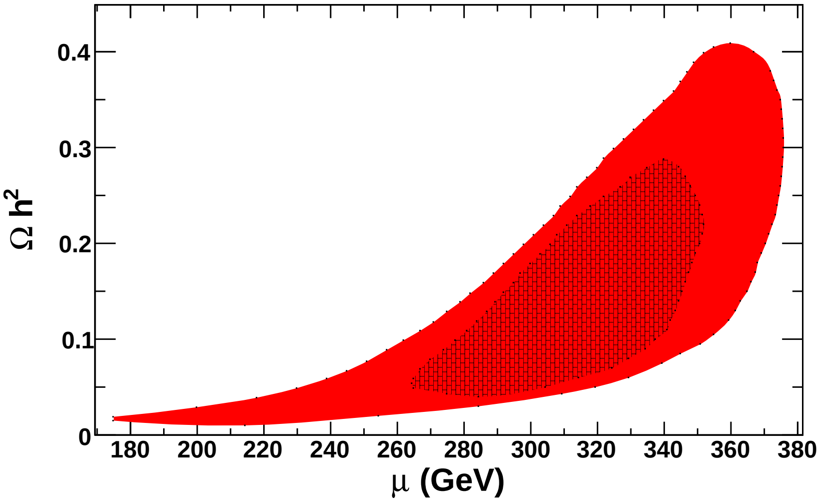

Figure 32: nuSUGRA Error Ellipse. The 1σ uncertainty contour in the μ-$\Omega_{\widetilde{\chi}_1^0}h^2$ plane for the nuSUGRA benchmark point. The solid red region is for an integrated luminosity of 100 fb^{-1}, whereas the brick textured region is for 1000 fb^{-1}.

$m_{J\tau\tau}^{\text{peak}} = f_3(m_{1/2}, m_H, m_0)$, $m_{\tau\tau}^{\text{end}} = f_4(m_{1/2}, m_H, m_0, A_0)$, and $m_{J\tau}^{\text{end}} = f_5(m_{1/2}, m_H, m_0, A_0, \tan\beta)$. We once again invert these functional forms for this region. Here, the inversion is easy, since the functional forms worked out in such a way that we can solve for one model parameter at a time. We only need to estimate the effect of the uncertainty in each parameter as we solve for the next. Simple Monte Carlo programs can once again help us with this task. The resulting parameters and their uncertainties we find for this benchmark point are shown in Table 11. It also shows the resulting uncertainty in the dark matter relic density found with DARKSUSY. In this region, the dark matter relic density is highly dependent on the value of μ. Thus, we also show the 1σ contour in the μ-$\Omega_{\widetilde{\chi}_1^0}h^2$ plane in Figure 32.

5 CONCLUSION

In this dissertation, we have examined signals of simple SUSY models at the LHC. We examined in particular the simple, four-parameter mSUGRA model. We also studied a natural generalization of mSUGRA, the nuSUGRA model. For these models, we showed some possible physical observables which can be used to identify the SUSY particle signals. We also showed how powerful background subtracting techniques can clean up those signals to make good measurements of the SUSY particle masses. The physical observables and subtraction techniques used were very general, and applicable to many other models as well. We discussed for various mSUGRA motivated models with dark matter candidates how the model can be fully reconstructed at the LHC using a model-dependent analysis.

Lastly, we have shown that all of these studies which use a model-dependent analysis at the LHC can provide an independent check of the dark matter relic density as measured by WMAP. Such a check is absolutely crucial to understanding the particle nature of dark matter and making the connection between particle physics and cosmology. There are many other dark matter motivated models where we can perform this check. It is very important to study these models as well in order to discriminate between the competing models of nature.

For instance, one of the other models under current investigation is the Mirage SUSY scenario [30]. This scenario is similar to mSUGRA in the sense that many of the SUSY particle masses are similar to each other at a high energy scale. However, the Mirage scale where this unification occurs can be much smaller than the unification scale of mSUGRA. This leads to a unique relation between the SUSY masses at the energy scale where we can measure them at the LHC. Thus, this Mirage SUSY model can be discriminated from the mSUGRA model. Also, this Mirage model has its own parameter space, as well as its own dark matter allowed regions. Studying the final states of these regions may uncover even more useful techniques for measuring new SUSY particles. This is currently under investigation.

In conclusion, the connection between particle physics and cosmology is pivotal for us to understand the particle nature of dark matter. In my studies, I have shown that simple dark matter motivated models of SUSY can be fully determined at the LHC. The model parameters can be used to infer the unmeasured SUSY masses and determine the dark matter relic density of the universe. The comparison of the relic density measured this way with the WMAP experiment will increase our understanding of dark matter and, thus, our entire universe.

REFERENCES

[1] WMAP Collaboration, D.N. Spergel *et al.*, Astrophys. J. Suppl. **148** (2003) 175.

[2] M. Markevitch, A. H. Gonzalez, L. David, A. Vikhlinin, S. Murray, *et al.*, Astrophys. J **567** (2002) L27; D. Clowe, A. Gonzalez, and M. Markevitch, Astrophys. J **604** (2004) 596; M. Markevitch, A. H. Gonzalez, D. Clowe, A. Vikhlinin, L. David, *et al.*, Astrophys. J **606** (2004) 819.

[3] S. Martin, arXiv:hep-ph/9709356.

[4] H. Goldberg, Phys. Rev. Lett. **50** (1983) 1419; J. Ellis, J. Hagelin, D. Nanopoulos, K. Olive, and M. Srednicki, Nucl. Phys. B **238** (1984) 453.

[5] D. Z. Freedman, P. Van Niewenhuisen, and S. Ferrara, Phys. Rev. D **13** (1976) 3214; S. Deser and B. Zumino, Phys. Lett. B **65** (1976) 369; A.H. Chamseddine, R. Arnowitt, and P. Nath, Phys. Rev. Lett. **49** (1982) 970; R. Barbieri, S. Ferrara, and C.A. Savoy, Phys. Lett. B **119** (1982) 343; L. Hall, J. Lykken, and S. Weinberg, Phys. Rev. D **27** (1983) 2359; P. Nath, R. Arnowitt, and A.H. Chamseddine, Nucl. Phys. B **227** (1983) 121; For a review, see P. Nilles, Phys. Rep. **110** (1984) 1.

[6] B. C. Allanach, G. A. Blair, S. Kraml, H.-U. Martyn, G. Polesello, *et al.*, [arXiv:hep-ph/0403133]; P. Bechtle, K. Desch, W. Porod, and P. Wienemann, Eur. Phys. J. C **46**, (2006) 533; R. Lafaye, T. Plehn, M. Rauch and D. Zerwas, Eur. Phys. J. C **54**, (2008) 617; J. L. Kneur and N. Sahoury, Phys. Rev. D **79**, (2009) 075010; C. Adam, J.-L. Kneur, R. Lafaye, T. Plehn, M. Rauch, *et al.*, [arXiv:hep-ph/1007.2190].

[7] "The ATLAS Experiment", 2011, `http://atlas.ch/`.

[8] "The Compact Muon Solenoid Experiment", 2011, `http://cms.web.cern.ch/cms/index.html`.

[9] E. Kolb and M. Turner, *The Early Universe* (Addison-Wesley Publishing Company, 1990).

[10] F. E. Paige, S. D. Protopopescu, H. Baer and X. Tata, [arXiv:hep-ph/0312045].

[11] T. Sjostrand, S. Mrenna, and P. Skands, J. High Energy Phys. **05** (2006) 026.

[12] "PGS 4", 2009, `http://www.physics.ucdavis.edu/~conway/research/software/pgs/pgs4-general.htm`.

[13] "ROOT", 2011, `http://root.cern.ch/drupal/`.

[14] P. Gondolo, J. Edsjo, P. Ullio, L. Bergstrom, M. Schelke, *et al.*, [arXiv:astro-ph/0211238].

[15] B. Allanach, C. Lester, M. Parker, and B. Webber, J. High Energy Phys. **09** (2000) 004.

[16] I. Hinchliffe, F. E. Paige, M. D. Shapiro, J. Söderqvist, and W. Yao, Phys. Rev. D **55** (1997) 5520; I. Hinchliffe and F. E. Paige, Phys. Rev. D **61** (2000) 095011.

[17] M.G. Albrow, B. Alper, J. Armitage, D. Aston, P. Benz, *et al.*, Nucl. Phys. B **114** (1976) 365; ATLAS Collaboration, N. Ozturk, [arXiv:hep-ph/0710.4546]; The CMS Collaboration, J. High Energy Phys **09** (2010) 091.

[18] M. Mangago, M. Moretti, F. Piccinini, R. Pittau, and A. Polosa, J. High Energy Phys **07** (2003) 001. We use ALPGEN version 2.13.

[19] CDF Collaboration, Phys. Rev. Lett. **105** (2010) 252001.

[20] J. Ellis, K. Olive, Y. Santoso, and V. Spanos, Phys. Lett. B **565** (2003) 176; R. Arnowitt, B. Dutta, and B. Hu, [arXiv:hep-ph/0310103]; H. Baer, C. Balazs, A. Beyaev, T. Krupovnickas, and X. Tata, J. High Energy Phys. **06** (2003) 054; B. Lahanas and D. Nanopoulos, Phys. Lett. B **568** (2003) 55; U. Chattopadhyay, A. Corsetti, and P. Nath, Phys. Rev. D **68** (2003) 035005; E. Baltz and P. Gondolo, J. High Energy Phys. **10** (2004) 052; A. Djouadi, M. Drees, and J.-L. Kneur, [arXiv:hep-ph/0602001].

[21] K. Griest and D Seckel, Phys. Rev. D **43** (1991) 3191.

[22] R. Arnowitt, B. Dutta, T. Kamon, N. Kolev, D. Toback *et al.*, Phys. Lett. B **639** (2006) 46.

[23] R. Arnowitt, B. Dutta, A. Gurrola, T. Kamon, A. Krislock, *et al.*, Phys. Rev. Lett. **100** (2008) 231802.

[24] I. Antoniadis, C. Bachas, J. R. Ellis, and D. V. Nanopoulos, Phys. Lett. B **211** (1988) 393; Nucl. Phys. B **328** (1989) 117; Phys. Lett. B **257** (1991) 278; J. R. Ellis, N.E. Mavromatos, and D. V. Nanopoulos, Lectures given at International Workshop on Recent Advances in the Superworld, Woodlands, TX, 13-16 Apr 1993, Published in Woodlands Superworld 1993:3-26 (QCD161:I966:1993) e-Print: hep-th/9311148; J. R. Ellis, N. E. Mavromatos, and D. V. Nanopoulos, Mod. Phys. Lett. A **10** (1995) 1685; Phys. Lett. B **619** (2005) 17.

[25] B. Dutta, A. Gurrola, T. Kamon, A. Krislock, A. B. Lahanas, *et al.*, Phys. Rev. D **79** (2009) 055002.

[26] K. L. Chan, U. Chattopadhyay, and P. Nath, Phys. Rev. D **58** (1998) 096004; J. L. Feng, K. T. Matchev, and T. Moroi, Phys. Rev. Lett. 84 (2000) 2322 and Phys. Rev. D **61** (2000) 075005; see also H. Baer, C. H. Chen, F. Paige, and X. Tata, Phys. Rev. D **52** (1995) 2746 and Phys. Rev. D **53** (1996) 6241; H. Baer, C. H. Chen, M. Drees, F. Paige, and X. Tata, Phys. Rev. D **59** (1999) 055014.

[27] "LHC Phenomenology Project 6: HB (or Focus Point)", 2009, `http://faculty.physics.tamu.edu/kamon/research/LHCpheno/LHC06/`

[28] H. Baer, A. Mustafayev, S. Profumo, A. Belyaev, and X. Tata, Phys. Rev. D **71** (2005) 095008 and J. High Energy Phys. **07** (2005) 065;

[29] B. Dutta, T. Kamon, A. Krislock, N. Kolev, and Y. Oh, Phys. Rev. D **82** (2010) 115009.

[30] K. Choi, K. Lee, Y. Shimizu, Y. Kim, and K. Okumura, J. Cosmology and Astroparticle Phys. **12** (2006) 017; H. Baer, E.-K. Park, X. Tata, and T. Wang, J. High Energy Phys. **08** (2006) 041.

VITA

Name: Abram Michael Krislock

Address: c/o Bhaskar Dutta
Department of Physics
Texas A&M University
4242 TAMU
College Station, TX 77843-4242

Education: B.S. Physics, University of Regina, 2004
Ph.D. Physics, Texas A&M University, 2011